Version R1

To be published in Acta Materialia

A Crystal Plasticity Investigation of Grain Size-Texture Interaction in Magnesium Alloys

Babak Ravaji[1*], Shailendra P. Joshi[1 †]

[1] Department of Mechanical Engineering, University of Houston, Houston, TX 77204-4006, USA

February 19, 2021

*Corresponding author: bravaji@uh.edu

†Corresponding author: shailendra@uh.edu

Abstract

This work investigates the microstructure-property linkages in magnesium (Mg) with an emphasis on understanding interaction effects between the grain size, texture, and loading orientation. A single crystal plasticity framework endowed with experimentally informed micro Hall-Petch type relations for the activation thresholds for slip and twinning is adopted to resolve polycrystalline microstructures over a broad texture-grain size space. The macroscopic trends from the simulations corroborate with experiments. The synergistic effects of microstructural engineering on the micromechanical characteristics are mapped, which reveal their role in the emergent macroscopic behaviors. The simulations predict reduced extension twinning with grain size refinement even though the micro Hall-Petch coefficient for twinning is smaller than that for the non-basal slip modes. While grain refinement and textural weakening generally reduce the net plastic anisotropy and tension-compression asymmetry, the degree to which these macroscopic behaviors are tempered depends on the loading orientation. The results offer a preliminary insight into the roles that texture and grain size may play in the damage behavior of engineered Mg microstructures.

Keywords: Hexagonal close-packed (HCP) materials, Magnesium (Mg) alloys, Grain-size effect, Textural variability, Crystal Plasticity.

Introduction

Owing to its low mass density and attractive mechanical properties, magnesium (Mg) alloys are potent candidates for a range of structural applications [1], from automotive components [2, 3] to biomedical implants [4]. However, the strength and failure properties of most Mg alloys fall short of aluminum (Al) alloys, which continue to be the preferred candidates in large-scale structural applications. It behooves materials scientists to adopt material design strategies to enhance the mechanical characteristics of Mg alloys [5].

Several conventional as well as novel strategies are investigated to engineer Mg microstructures with enhanced yield strength and strain hardening. These include: grain size refinement [6–11], alloy engineering for solute [12–14] and precipitate [12, 15, 16] strengthening, nanostructured [17, 18], hierarchical composites [19], texture modification [8], and combinations thereof.

Grain size strengthening, commonly referred to as the Hall-Petch effect [20, 21], is associated with the resistance offered by grain boundaries to the crystallographic deformation mechanisms. The empirical Hall-Petch relation for yield stress, σ_y, for a given average grain size $\bar{d}$ is: $\sigma_y = \sigma_0 + k_y \bar{d}^{-1/2}$ is an aggregate effect at the polycrystal scale due to the hardening of the individual deformation systems at the grain scale. There exist a number of experimental reports aimed at harnessing grain size effects in polycrystalline hexagonal close-packed (HCP) materials, particularly Mg and its alloys [e.g. 6–11, 22, 23]. However, HCP materials present a rich landscape of deformation systems and modes, each of which may exhibit different levels of hardening from their interactions with grain boundaries. Moreover, their low crystal symmetry also results in a more governing role of the material texture in the macroscopic plastic anisotropy, as evidenced in polycrystalline Mg and its alloys. By way of consequence, in these materials the aggregate effect of the interaction between the grain size and material texture is expected to be complicated [24–27]. While grain refinement leads to an increase in the yield stress, texture weakening tends to decrease it, see [28]. As a result, the interaction between the texture and grain size determines the overall strengthening [29–31], although assessing the quantitative nature of this interaction is not trivial [32]. Indeed, there exists ~~a good deal~~ of variability in the reports on grain size effects in same Mg alloys subjected to different thermo-mechanical processes, which makes it difficult to reliably predict their macroscopic responses [7, 33]. The situation may become even more complicated with

different rates and states of loading [34–38].

A particularly interesting aspect is the role of grain size in extension twinning. A number of studies demonstrate a reduced propensity to twinning with grain size refinement [39–43]. In rolled AZ31 alloys [25], extension twinning has been shown to decrease with decreasing grain size in both rolling (L) and in-plane transverse-to-rolling (T) directions with the amount of twinning being higher in the former than the latter. Furthermore, extension twinning may occur even under conditions that do not favor it. A recent insightful study [44] reveals that for a fixed initial texture the grain size effect on twinning in pure titanium is much stronger than in pure Mg, which contrasts with a similar previous study [32] that indicates the opposite. On the other hand, the dependence of average twin thickness on grain size is consistent in these works with titanium exhibiting a stronger effect than magnesium. In the context of a Hall-Petch type characterization, the grain size effect on twinning manifests in the form of a power-law relation for macroscopic yield stress: $\sigma_y = \sigma_0 + k_y \bar{d}^{-n}$. Akin to the Hall-Petch relation for slip, $n = 1/2$ has been generally been shown to corroborate well for extension twinning [41, 45, 46], although some works indicate $n \sim 1$ [47–49]. A more prevalent argument is that the Hall-Petch coefficient for twinning (k_y^t) should be larger than that for slip (k_y^s), which may be rationalized using scaling arguments and the number density of twins per unit grain volume [50]. Discrete dislocation dynamics simulations attribute a stronger grain size effect in extension twinning compared to slip [48] to sharper decrease in the twinning dislocation activity with grain refinement compared to matrix dislocation activity, albeit at high strain rates ($\sim 5000\ \mathrm{s}^{-1}$). Yet, quasi-static experiments reveal that at the crystallographic scale the grain size effect on the twinning critical resolved shear stress may not necessarily be stronger than on slip [51]. A recent experimental study on AZ31 rolled plates and extruded rods [40] highlights the role of texture in grain size strengthening; in extruded rods $(k_y^s)_{\mathrm{rod}} \ll (k_y^t)_{\mathrm{rod}}$ while in rolled plates $(k_y^s)_{\mathrm{plate}} \gg (k_y^t)_{\mathrm{plate}}$. It should be noted that these observations are based on loading along the specific directions (TD for plates and ED for rods).

While theoretical models provide useful insights into the role of individual strengthening mechanisms [32, 52, 53], their interacting effects are generally not well understood. A recent noteworthy effort in this direction [27] proposes a dislocation pile-up model to predict the effect of texture on the Hall-Petch behavior of Mg alloys. It appeals to the coupling between the intergranular misorientation between different deformation systems in neighboring grains and a

weighted difference in their activation stresses. Although the model shows good corroboration with experimental results that are dominated by the basal and prismatic slip modes, the predictions for twinning dominated behaviors are poor. An alternative approach, which relies on computational modeling provides a useful basis to shed light on the interacting effects between the different strengthening mechanisms. A grain size-dependent viscoplastic self-consistent (VPSC) polycrystal plasticity investigation by Agnew and colleagues [25, 54] indicates that the tensile responses of a rolled Mg alloy are primarily governed by the grain size dependence of the prismatic slip. By adopting a statistics-based model, Beyerlein et al. [55] extracted a strong relationship between grain size and twin density, while also explaining a weak correlation between the grain orientation and twin variant selection. VPSC-type calculations indicate the role of grain size in twin growth [56] as well as twin density [44] due to intergranular interactions that affect stress-fields within individual twin lamellas. As anticipated, these interactions depend on crystallographic orientations and intrinsic crystallographic elasto-plastic anisotropy.

A promising computational approach to understand the grain size-texture interactions is to adopt a finite element based polycrystal modeling based on a single crystal plasticity constitutive framework, which explicitly resolves the grain structure and texture. In this setting, one needs to incorporate a length-scale feature at the single crystal scale that manifests as a grain size effect at the polycrystalline scale. At the grain-scale, strengthening of a slip system arises from the barriers to dislocation slip offered by grain boundaries. In modeling explicit polycrystalline microstructures based on single crystal plasticity, this behavior can be rigorously incorporated by allowing the current slip and twin system strengths to depend on the gradients of strain and the ~~rate of strain~~, [cf. 57]. With this, a size effect naturally kicks in with decreasing grain size by virtue of the larger strain gradients for a given level of ~~intra-granular strain~~. However, such an approach is computationally rather expensive and becomes intractable even for a statistical volume ensemble (SVE) comprising a few grains. Another, somewhat less expensive alternative is to model grain boundaries as *interphases* of small, but fixed finite thickness with crystallographic resistances that are different from those of their bulk counterparts, which induce a grain size effect in the macroscopic stress by virtue of the increased grain boundary volume fraction with decreasing grain size [58]. One difficulty in this approach is to rationalize the strength parameters of the interphase as a function of the grain boundary character. Further, the approach may still end up being computationally

demanding because of the need to resolve interphases with fine finite element meshes.

In this paper, we investigate the grain size-texture interaction by adopting a single crystal plasticity approach to model realistic polycrystalline SVEs. The underlying HCP single crystal plasticity framework [59] has been applied to understand the micro-macro relationships in single as well as poly-crystalline systems, including nanoindentation behaviors [60], composites [61], void growth and coalescence [62], and structural responses of notched bars [63–65]. A very recent work [66] adopts the framework to investigate textural variability effects in the three-dimensional anisotropic responses of pure Mg and an Mg alloy. One highlight of that work is the prediction of the role of crystallographic and textural anisotropy in the damage tolerance. However, the foregoing investigations are size-independent as the underlying single crystal constitutive framework does not incorporate a material length-scale [59]. To account for the grain size effect, here we propose a modification to the constitutive model in the form of *micro* Hall-Petch type relations at the level of individual slip and twin systems. We perform detailed polycrystal simulations using the size-dependent crystal plasticity to understand the effect of texture on the grain size dependent behaviors. The simulations are performed under uniaxial tensile and compressive loading along the principal material directions of plastic anisotropy to quantify loading orientation dependence. Three different textures and four grain sizes (μm to mm) spanning a broad range of textural-grain size space are considered.

Modeling Approach

In this section, we briefly present a size-dependent crystal plasticity model that builds upon the basic framework of Zhang and Joshi [59]. We describe the polycrystal SVE along with textures that cover a broad range of microstructures, and the finite element representation including prescribed boundary conditions.

2.1 Crystal Plasticity Relations

The total velocity gradient ($\mathbf{L}$) in the deformed configuration is divided into elastic ($\mathbf{L}^e$) and plastic ($\mathbf{L}^p$) parts:

$$\mathbf{L} = \dot{\mathbf{F}}\mathbf{F}^{-1} = \mathbf{L}^e + \mathbf{L}^p \tag{1}$$

where $\mathbf{F}$ is the total deformation gradient. The plastic part of the velocity gradient is decomposed into two parts:

$$\mathbf{L}^p = \underbrace{\left(1 - \sum_{\beta=1}^{N_{tw}} f^\beta\right) \sum_{\alpha=1}^{N_s} \dot{\gamma}^\alpha (\mathbf{s}^\alpha \otimes \mathbf{m}^\alpha)}_{slip\ in\ parent} + \underbrace{\sum_{\beta=1}^{N_{tw}} \dot{\gamma}^\beta (\mathbf{s}^\beta \otimes \mathbf{m}^\beta)}_{twin\ in\ parent} \tag{2}$$

where $\dot{\gamma}$ is the shear strain rate, superscript α and β represent slip and twin modes respectively, $\mathbf{s}^i$ the slip ($i = \alpha$) or twin ($i = \beta$) direction and $\mathbf{m}^i$ their respective plane normals. Here, $N_s = 18$ are the total number of the slip systems, which includes basal (3), prismatic (3), pyramidal $\langle a \rangle$ (6), and pyramidal $\langle c + a \rangle$ (6) modes; $N_{tw} = 12$, which include six extension twin (ET) and six contraction twin (CT) modes. In Eq. (2), f^β denotes the current twin volume fraction on the twin system β.

The rates of slip ($\dot{\gamma}^\alpha$) and twinning ($\dot{\gamma}^\beta$) are defined as follows:

$$\dot{\gamma}^\alpha = \dot{\gamma}_0 \left| \frac{\tau^\alpha}{g^\alpha} \right|^{1/m} \text{sign}(\tau^\alpha) \qquad ; \qquad \dot{\gamma}^\beta = \dot{f}^\beta \gamma^{tw} \tag{3}$$

with $\dot{\gamma}_0$ being the reference slip rate, and γ^{tw} the constant twinning shear for a given twin mode [67], and m is the single crystal rate-sensitivity parameter for slip. In Mg, $\gamma^{tw} = 0.129$ for extension twinning and $\gamma^{tw} = 0.138$ for contraction twinning. In Eq. $(3)_1$, τ^α is the current resolved shear stress (RSS) on the slip system α, and g^α is the current slip system resistance that evolves with deformation as:

$$g^\alpha = \tau_0^\alpha + \int_{t_0}^{t} (\dot{g}_{sl-sl}^\alpha + \dot{g}_{tw-sl}^\alpha)\, \mathrm{d}t \tag{4}$$

where τ_0^i is the initial critical resolved shear stress (CRSS). $\dot{g}_{sl-sl}^i$ and $\dot{g}_{tw-sl}^i$ denote the hardening rates on i^{th} slip system due to slip-slip and slip-twin interactions, respectively:

$$\dot{g}_{sl-sl}^i = \sum_{j=1}^{N_s} h_{ij}(\bar{\gamma}) \dot{\gamma}^j \quad , \qquad h_{ij} = \begin{cases} h(\bar{\gamma}) & (i = j \text{ self hardening}) \\ q h(\bar{\gamma}) & (i \neq j \text{ latent hardening}) \end{cases} \tag{5}$$

where $\bar{\gamma}$ is the accumulated shear on all slip systems, h_{ij} are the self ($i = j$) and latent ($i \neq j$) hardening moduli, and q the latent hardening coefficient (set equal to 1 for simplicity). Based on experimental evidence, the hardening evolution of basal slip is of the non-saturation type whereas non-basal slip hardening exhibits a saturation behavior [59]. Thus, the corresponding phenomeno-

logical evolution functions are chosen as:

$$h(\bar{\gamma}) = \begin{cases} h_0, & \text{(basal slip)} \\ h_0^i \ \text{sech}^2 \left| \frac{h_0^i \bar{\gamma}}{\tau_s^i - \tau_0^i} \right|, & \text{(non-basal slip)} \end{cases} \tag{6}$$

where h_0 is the initial slip hardening modulus and τ_s is the saturation stress. The hardening rates of slip resistances due to interactions with extension and contraction twinning are chosen as:

$$\dot{g}_{tw-sl}^{\alpha} = \begin{cases} h_{et\_sl}^{\alpha} \ \text{sech}^2 \left| \frac{h_{et\_sl}^{\beta} \bar{\gamma}_{et}}{\tau_{s\_et}^{\beta} - \tau_{0\_et}^{\beta}} \right| \dot{\gamma}^{ET}, & \text{(ET)} \\ 0.5 H_{ct\_sl} (\bar{\gamma}_{ct})^{-0.5} \dot{\gamma}^{CT}, & \text{(CT)} \end{cases} \tag{7}$$

depicting a saturation hardening for the slip due to rapid evolution of ET with a hardening modulus h_{et-sl} and a non-saturation type hardening (hardening modulus H_{ct-sl}) of the slip due to thin CTs that act as a barrier to dislocation motion [59].

For twinning modes, the evolution of twin volume fraction ($\dot{f}^{\beta}$) in Eq. $(3)_2$ is defined by power-law functions with a rate sensitivity parameter m_t:

$$\dot{f}^{\beta} = \begin{cases} \dot{f}_{et}^{0} \left(\tau^{\beta} / s_{et}^{\beta} \right)^{1/m_t}, & \text{(ET)} \\ \dot{f}_{ct}^{0} \left(\tau^{\beta} / s_{ct}^{\beta} \right)^{1/m_t}, & \text{(CT)} \end{cases} \tag{8}$$

Here, $\dot{f}_{et}^{0}$ and $\dot{f}_{et}^{0}$ are the characteristic rates of ET and CT volume fraction and s_{I}^{β} is the twin system resistance for the twin mode $\text{I} = \text{ET}, \text{CT}$ computed as follows:

$$s^{\beta} = \tau_0^{\beta} + \int_{t_\circ}^{t_i} (\dot{s}_{tw-tw}^{\beta} + \dot{s}_{sl-tw}^{\beta}) \, \mathrm{d}t \tag{9}$$

where the twin-twin interactions for ET and CT are as follows:

$$\dot{s}_{tw-tw}^{\beta} = h_{\text{et}}^{\beta} \ \text{sech}^2 \left| \frac{h_{\text{et}}^{\beta} \bar{\gamma}_{et}}{\tau_{s\_et}^{\beta} - \tau_{0\_et}^{\beta}} \right| \dot{\gamma}^{\beta} \quad , \qquad \dot{s}_{tw-tw}^{\beta} = H_{ct} \left(\sum_{m=1}^{N_{ct}} f^m \right)^b \dot{\gamma}^{\beta} \tag{10}$$

which respectively represent a propensity of ET volume fraction to easy growth and, in contrast, the high resistance of CTs to nucleation and growth [59]. In Eq. (10), $h_{\text{et}}^{\beta}, \tau_{0\_et}^{\beta}$ and $\tau_{s\_et}^{\beta}$ respectively

denote the initial hardening modulus, CRSS, and saturation stress for the given ET system β. Likewise, $\tau^{\beta}_{0\_et}$ and b control the hardening rate of the CT system β. We assume that slip evolution does not affect twin hardening, i.e. in Eq. (9), $\dot{s}^{\beta}_{sl-tw} = 0$ [59].

At a given time t, the accumulated extension twin volume fraction at each Gauss point $f^{\mathrm{ET}}(t)$ and its volume-averaged representation $\bar{f}^{\mathrm{ET}}(t)$ is:

$$f^{\mathrm{ET}}(t) = \sum_{\beta=1}^{6} f^{\beta}(t) \qquad ; \qquad \bar{f}^{\mathrm{ET}}(t) = \frac{1}{V}\int f^{\mathrm{ET}}(t)\ \mathrm{dV} \tag{11}$$

Computationally, when $f^{\mathrm{ET}} = f_{\mathrm{cr}}$ (we set $f_{\mathrm{cr}} = 0.9$ [59]) at a Gauss point the corresponding element volume is reoriented to the twinned orientation of the variant β that has the largest contribution. Upon reorientation, the f^{ET} at the particular Gauss point is reset to zero. Therefore, $0 \leq \bar{f}^{\mathrm{ET}}(t) \leq 1$. A twinned region in a grain becomes a new sub-grain that plastically deforms slip and/or twinning (i.e. double twinning is possible). The same approach is adopted for contraction twinning.

The foregoing relations do not embed any internal microstructural length-scale and therefore, they constitute a size-independent behavior. Here, we modify certain constitutive descriptors to incorporate a grain size effect in the slip and twinning resistances, described next. Consider a polycrystal microstructure in (Fig. 1a) with a grain size distribution (Fig. 1b). We calculate the equivalent grain diameter d_{eq} for each grain. Then, for each grain, we express the initial CRSS τ^{i}_{0} (cf. Eq. (4) and (9)) of a deformation system $i = (\alpha, \beta)$ as [25, 54]:

$$\tau^{i}_{0} = \bar{\tau}^{i}_{0} + k^{i}_{\tau}(d_{\mathrm{eq}})^{-1/2} \tag{12}$$

Here, $\bar{\tau}^{i}_{0}$ denotes a size-independent CRSS (for large single crystals) for the i^{th} system, and k^{i}_{τ} is a Hall-Petch type parameter defined for the particular deformation system.

The saturation stresses τ_s for slip (Eq. (6)) and twinning (Eq. (10)) are also assumed to depend on the grain size. This assumption stems from the fact that stress saturation is a result of saturation of the overall dislocation density – a consequence of trapping, annihilation and recovery of the mobile and immobile dislocations [68, 69]. For severely plastically deformed bulk microstructures, the initial dislocation density generally increases with grain size refinement [70, 71]

and thus, a similar trend is anticipated for the saturation stress as well. However, such a detailed experimental characterization of the flow stress saturation in HCP materials is not readily available. On the other hand, experiments and detailed theoretical as well as computational modeling of FCC materials indicate that the rate at which the flow stress changes is inversely proportional to grain size. The proportionality typically lies between $d^{-1/2}$ to d^{-1} but closer to the latter [72–75]. Based on these accounts, we assume that:

$$\tau_s^i = \bar{\tau}_s^i + k_s^i (d_{\text{eq}})^{-1}, \qquad \tau_s^i \geq \tau_0^i \tag{13}$$

where $\bar{\tau}_s^i$ is the size-independent saturation stress of a single crystal for the deformation system i, and k_s^i (discussed *et seq.*) is a proportionality factor akin to the k_τ in Eq. (12). Note that the saturation stress should be an upper bound of the flow stress and hence, larger than the initial CRSS. As such, from a computational standpoint we set a limiting condition that, for an i^{th} system $\tau_s^i = \tau_0^i$ if $\tau_s^i < \tau_0^i$.

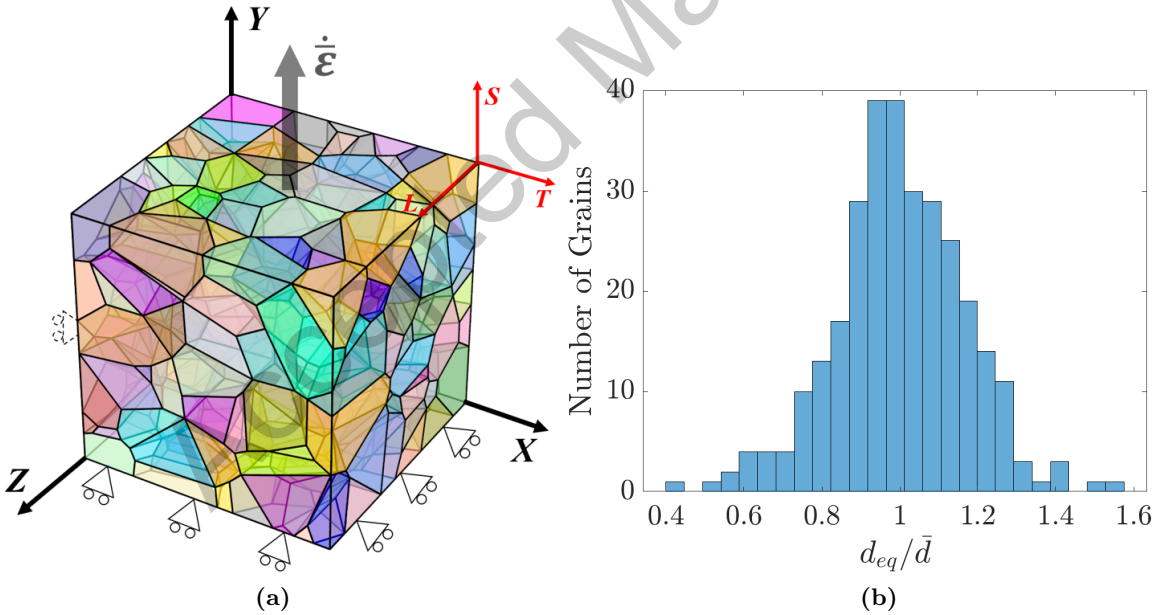

Figure 1 (a) Setup of polycrystal statistical volume element (SVE) with kinematic boundary conditions, and (b) corresponding grain size distribution.

Table 1 Material parameters for Mg alloy AZ31 [63, 64, 76–79]

Mechanisms	$\bar{\tau}_0$ (MPa)	h_0 (MPa)	$\bar{\tau}_s$ (MPa)	
Basal	10	50	-	
Prismatic	55	1500	110	
Pyramidal $\langle a \rangle$	55	1500	110	
Pyramidal $\langle c+a \rangle$	60	3000	170	
	$\bar{\tau}_0$ (MPa)	h_{et} (MPa)	τ_{s_et} (MPa)	h_{et_sl} (MPa)
Extension twinning	15	120	30	100
	$\bar{\tau}_0$ (MPa)	H_{ct} (MPa)	H_{ct_sl} (MPa)	b
Contraction twinning	85	6000	15	0.05

2.2 Finite Element Model

With the size-dependent constitutive model in place, Fig. 1 shows the three-dimensional polycrystal microstructure with a normal grain size distribution generated using NEPER [80]. The microstructure comprises 300 grains, and each grain is discretized using a fine mesh of tetrahedral finite elements (C3D4 in ABAQUS). Each grain is identified by a set of Euler angles with respect to a reference orientation. To begin, a reference single crystal orientation is defined such that the three crystallographic directions $[1\bar{2}10], [10\bar{1}0]$ and $[0001]$ are respectively aligned with the material axes L-T-S. Then, based on the desired texture the crystal orientation of each grain is rotated using the Bunge scheme. In the present work, we represent a texture by the maximum standard deviations of each Euler angle. Thus, given a mean Euler angle set $[\varphi_1, \Phi, \varphi_2]$, a particular texture is denoted by $[E^\varsigma] = [\pm\varphi_1^\varsigma, \pm\Phi^\varsigma, \pm\varphi_2^\varsigma]$ where the superscript ς indicates that these are standard deviations of the respective Euler angles. In this work, we consider three cases: texture B ($[E^\varsigma] = [10°, 15°, 0°]$), texture E ($[E^\varsigma] = [30°, 20°, 0°]$), and texture K ($[E^\varsigma] = [45°, 75°, 45°]$). Fig. 2 shows the corresponding pole figures plotted using MTEX [81]. These three cases are a subset of the range of textures considered by Indurkar et al. [66], and for consistency with that work we retain their labels B, E, and K. Texture B is a strong texture not very different from the limiting case of a single crystal; texture E is an intermediate texture representative of a typical experimental rolling texture [82, 83]; finally, texture K is much weaker, resembling a randomly textured polycrystal [84], e.g. that in a cast Mg alloy. As such, these sampled textures cover a broader spectrum of experimental textures with the hope of enabling design guidelines via texture-grain size interaction effects.

As shown in Fig. 1a, the microstructure is loaded under a uniaxial tensile or compressive boundary condition by applying a constant nominal strain rate ($\dot{\bar{\varepsilon}}$) along the Y-axis. In general, the L-T-S frame may be arbitrarily oriented with the laboratory frame (X-Y-Z); for convenience, here we restrict our attention to the loading states where L-T-S is aligned with X-Y-Z. We consider loading along the three principal material axes. Fig. 1a shows a particular case where the material S-direction is aligned with the Y-axis and is under tensile loading; we refer to this case as S-tension. To obtain a response along another material direction, the Euler angles of each grain are rotated appropriately. For example, loading along the T-axis is accomplished by rotating the Euler angles such that the T-axis is aligned along the Y-axis. Symmetry boundary conditions are applied on the bottom XZ plane, and left YZ plane. Further, all the three displacements at the origin (X=Y=Z=0) are constrained to ensure no rigid motions.

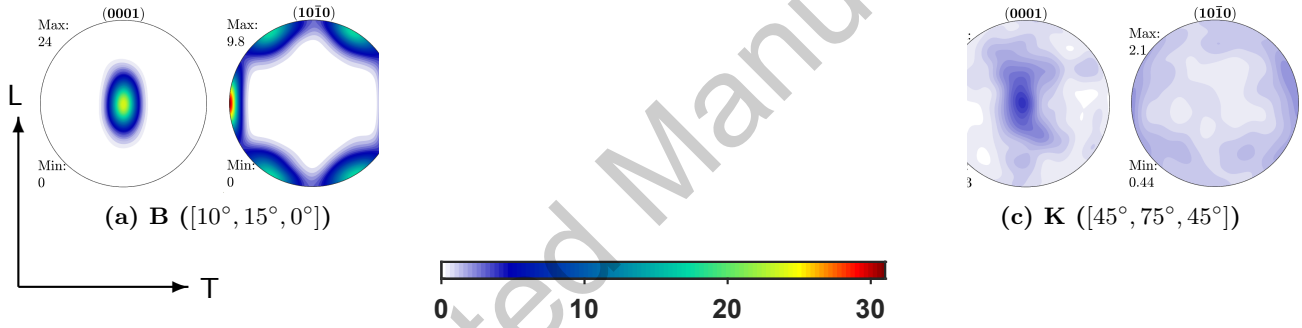

Figure 2 The initial [0001] and [10$\bar{1}$0] pole figures projected on the LT plane for textures B (strong), E (intermediate), and K (weak). The third principal material direction, S, is normal to the plane. The respective maximum variations of the three Euler angles are shown in brackets. Texture B represents a strong texture, akin to a single crystal texture, the intermediate texture E represents typical rolled textures, and texture K is the weakest, representing a random polycrystal texture.

Table 2 The Hall-Petch parameters for each individual deformation mode of the Mg alloy AZ31.

	Basal	Prismatic	Pyramidal $\langle a \rangle$	Pyramidal $\langle c+a \rangle$	Extension Twin	Contraction Twin
k_τ (MPa μm$^{1/2}$)	83 [51]	175 [51]	272 [51]	272	180 [51]	272

Table 1 consolidates the size-independent material parameters [66]. In addition, we set $\dot{\gamma}_0 = 0.001$ s^{-1} for all slip modes. For twinning, we set $\dot{f}^0_{et} = 0.001$ s^{-1} (extension twinning) and $\dot{f}^0_{ct} = 0.0001$ s^{-1} (contraction twinning). The strain rate sensitivity parameters for the slip and

twin modes are $m = m_t = 0.02$. Table 2 consolidates the k_τ values for different slip and twin system. A very recent work [85] indicates that k_τ^{basal} depends on the grain boundary character. However, here we assume all the crystallographic Hall-Petch coefficients to be constants. Barring the pyramidal $\langle c+a \rangle$ slip and contraction twin, the k_τ values for other modes are adopted from those obtained by Wang and Choo [51] via a systematic set of experiments for a particular texture. For the pyramidal $\langle c+a \rangle$ slip and contraction twinning we assume that the grain size induced hardening is similar to the pyramidal $\langle a \rangle$ mode. On the other hand, the factor k_s^i in Eq. (13) is not readily obtained from the experiments but can be estimated as $k_s^i \equiv \zeta \mu b^i$ [73] , where μ is the shear modulus, b^i the magnitude of Burgers vector for i^{th} deformation system, and $3 \lesssim \zeta \lesssim 10$ [73, 86]. Using typical values for Mg alloys, we adopt a single value for k_s^i as $k_s = 200$ MPa.μm. We note here that these material parameters are not calibrated against any specific set of experiments. They are representative of a typical AZ31 alloy single crystal.

The volume-averaged state of macroscopic true stress due to an applied nominal strain-rate ($\dot{\bar{\varepsilon}}$) along the Y-axis is $\boldsymbol{\sigma} = \sigma_{yy} (\mathbf{e}_y \otimes \mathbf{e}_y)$, where $\mathbf{e}_y$ is the unit vector along the Y-direction. The macroscopic true strain is defined as: $\boldsymbol{\varepsilon} = \varepsilon_{xx} (\mathbf{e}_x \otimes \mathbf{e}_x) + \varepsilon_{yy} (\mathbf{e}_y \otimes \mathbf{e}_y) + \varepsilon_{zz} (\mathbf{e}_z \otimes \mathbf{e}_z)$, with $\varepsilon_{xx} = \ln (L_x/L_0)$, $\varepsilon_{yy} = \ln (L_y/L_0)$ and $\varepsilon_{zz} = \ln (L_z/L_0)$. The von Mises equivalent stress and the corresponding effective strain are: $\sigma_{eq} = \sqrt{(3/2)\boldsymbol{\sigma}' : \boldsymbol{\sigma}'} = |\sigma_{yy}|$ and $\varepsilon_{eq} = \sqrt{(2/3)\boldsymbol{\varepsilon}' : \boldsymbol{\varepsilon}'}$ where $\boldsymbol{\sigma}'$ and $\boldsymbol{\varepsilon}'$ are the deviatoric stresses and strains respectively.

Results

To investigate the grain size effect, we consider three average grain sizes $\bar{d} = 180$ μm, 18 μm, and 1.8 μm. In addition, we also perform the same set of simulations with no grain size effect (hereafter referred to as the base material). For a consistent comparison, the same microstructure and grain size distributions is adopted (Fig. 1). In all the simulations, we set $\dot{\bar{\varepsilon}} = 1 \times 10^{-3}$ s^{-1}.

3.1 Macroscopic Uniaxial Tensile Responses

Fig. 3 depicts the grain size effect on the uniaxial tensile responses for the three textures when loaded along the principal axes. Fig. 3a, 3c, and 3e show the full stress-strain responses for loading along the L, T, and S directions, respectively. Fig. 3b, 3d, and 3f are the corresponding Hall-Petch

plots consolidating the texture dependent grain size effect on the macroscopic yield strength. In the stress-strain plots, the base material denotes the response for a given texture with no grain size effect. For clarity, the $\bar{d}$=180 μm are omitted from the stress-strain plots; they are included in the Hall-Petch plots.

The stress-strain responses reveal several salient features. It is expected that the responses in L-tension and T-tension are dominated by non-basal slip whereas S-tension is governed by extension twinning [66]. Against that backdrop, for a given loading direction the grain size effect is different for different textures. Further, for the same texture the grain size effect can be different when loaded along different directions, even under slip-dominated loading conditions (cf. Fig. 3a and 3e). The Hall-Petch plots (Fig. 3b, 3d, and 3f) further clarify these features in the context of the initial yield stress (σ_y), defined here as the stress corresponding to 0.2% proof strain. The discrete data obtained the different grain sizes are fitted to the Hall-Petch expression $\sigma_y = \sigma_0 + k_y(\bar{d})^{-1/2}$ where σ_0 is the yield stress of the base material, and k_y is the effective Hall-Petch parameter. Table 3 summarizes the Hall-Petch parameters for the three textures when loaded in tension along the L, T, and S directions. As can be seen, the general trend is that the yield stress along a particular loading direction increases more rapidly with decreasing grain size if the initial texture is stronger. We note that texture plays a stronger role in the Hall-Petch characteristics for T-tension compared to L-tension despite both responses being dominated by slip mechanisms. In other words, for slip-dominated tensile loading states the grain size-texture interaction effect on the initial yield stress depends on the loading direction.

The computed values for $k_y \sim$ 257-370 MPa μm$^{1/2}$ are reasonably close to the experimentally reported range $\sim$ 208-348 MPa μm$^{1/2}$ [25, 87–90], particularly considering that the model is not calibrated to any particular experimental dataset.

For S-tension (Fig. 3e), the responses exhibit a sigmoidal behavior for textures B and E, which is a characteristic of profuse extension twinning. Notably, even in the fine-grained material ($\bar{d} = 1.8$ μm) the sigmoidal characteristic is observed indicating that extension twinning is active. In comparison, texture K shows a more power-law type behavior at all grain sizes (including the base material) suggesting that extension twinning may not be dominant (we discuss these aspects in Section 3.3). Despite these differences, the corresponding Hall-Petch plot (Fig. 3f) is relatively insensitive to the initial texture. In other words, grain size and texture are weakly coupled at initial

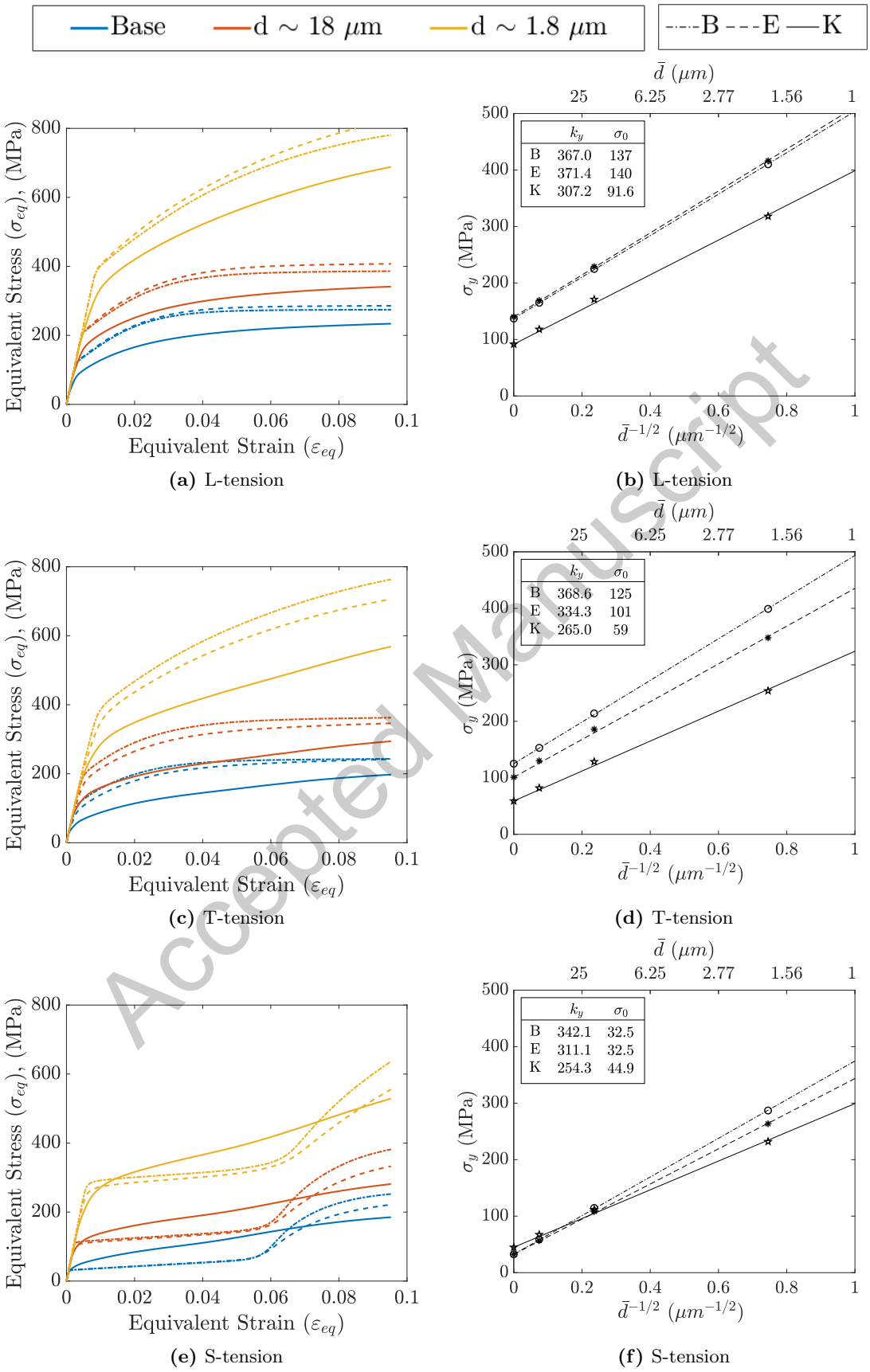

(a) L-tension **(b)** L-tension

(c) T-tension **(d)** T-tension

(e) S-tension **(f)** S-tension

Figure 3 Uniaxial tensile responses along principal material directions L, T, and S. Panels (a, c, e) show the equivalent stress-equivalent strain curves as a function of grain size and texture under different loading orientations. Panels (b, d, f) collate the corresponding initial yield stresses in the form of Hall-Petch plots.

yield under twinning-dominated tensile loading.

The flow stress evolution under tensile loading reveals a grain size dependence as well. Under L- and T-tension, the flow stresses tend to saturate at relatively moderate strains ($\bar{\varepsilon}_{eq} \sim 0.06 - 0.08$) for larger grain sizes (base material, $\bar{d} = 180$, and 18 μm), and this is particularly the case for textures B and E, and to a lesser extent for the weakest texture (K). On the other hand, the responses for $\bar{d} = 1.8$ μm tend to show a delayed trend toward flow stress saturation. For S-tension, the flow stresses for the larger grain sizes and stronger textures (B, E) tend to saturate immediately after the twinning-induced hardening. In comparison, for $\bar{d} = 1.8$ μm (for all textures) as well as for the texture K (at all grain sizes), the flow stress continues to evolve well beyond the twinning-induced hardening. It is interesting to note the $\sigma_f - \bar{d}^n$ dependence. At $\varepsilon_{eq} \sim 0.1$, we obtain $n \sim -0.42$ for twinning-dominated loading cases and $n \sim -0.64$ for slip-dominated loading cases.

Table 3 The effective Hall-Petch parameters for the Mg alloy AZ31 under **tensile** boundary conditions with respect to material texture and loading direction.

	B $[10°, 15°, 0°]$			E $[30°, 20°, 0°]$			K $[45°, 75°, 45°]$		
	L	T	S	L	T	S	L	T	S
k_y (MPa μm$^{1/2}$)	368.1	366.2	341.5	370.3	329.3	311.2	305.9	258.2	257.9
σ_0 (MPa)	136	124	33	140	101	33	92	60	45

3.2 Macroscopic Uniaxial Compressive Responses

Fig. 4 consolidates the results for the grain size and texture-dependent responses when loaded in uniaxial compression along the same principal directions. As expected, a compressive loading along the L- and T-axes results in the emergence of the sigmoidal stress-strain response indicative of extension twinning akin to S-tension. However, there are several subtle differences in these responses relative to the S-tension. A particularly interesting result pertains to L-compression, Fig. 4a, which reveals that the sigmoidal responses for the textures B and E are much tempered compared to their counterparts in T-compression and S-tension. This observation is qualitatively consistent with the compressive responses of equal channel angular extruded AZ31B Mg alloys reported by Foley et al. [31]. Moreover, at $\bar{d} = 1.8$ μm the texture B (strongest of the three textures) exhibits a depleted hardening. In fact, its is virtually indiscernible from that of texture

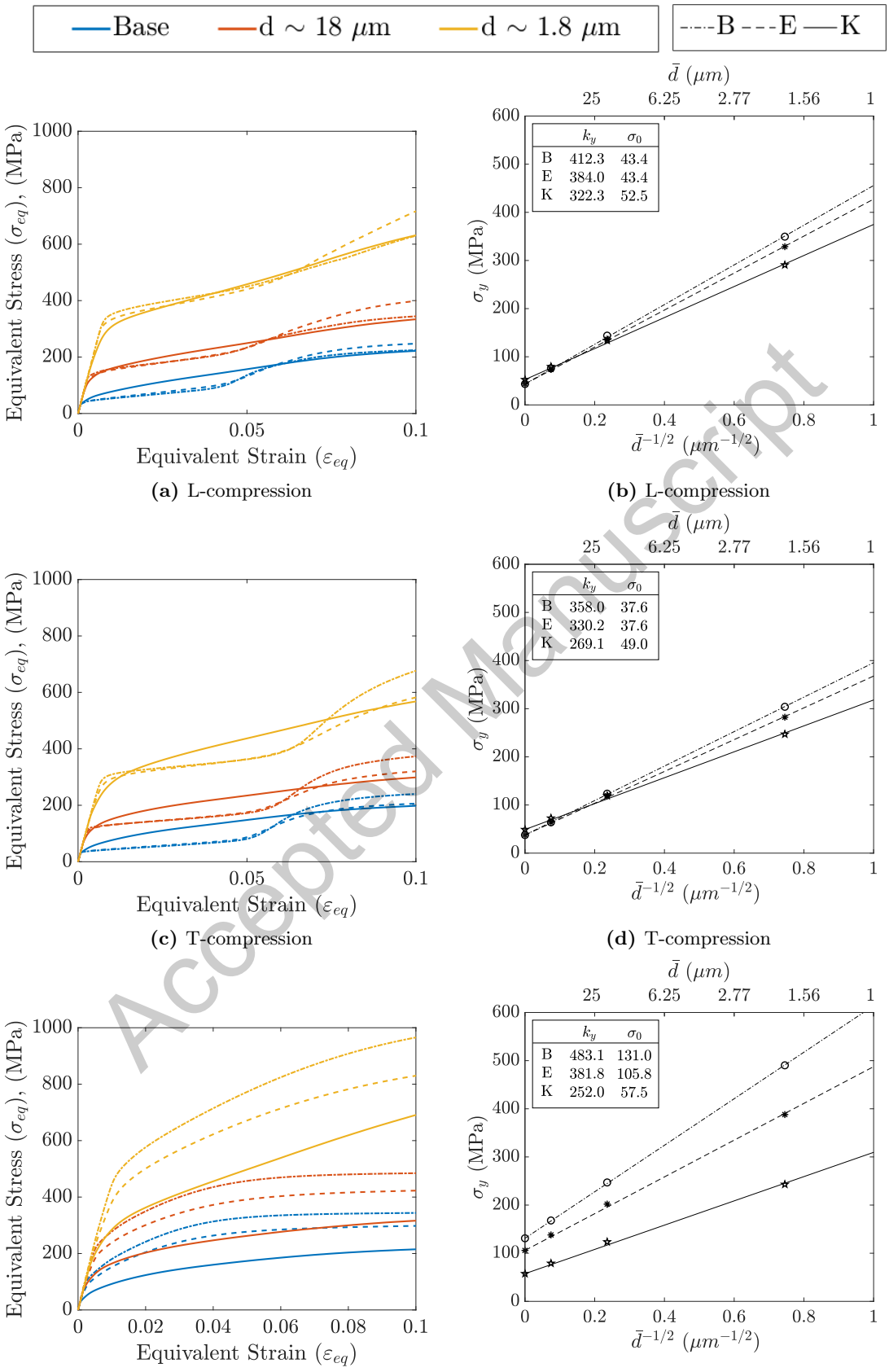

(a) L-compression **(b)** L-compression

(c) T-compression **(d)** T-compression

(e) S-compression **(f)** S-compression

Figure 4 Uniaxial compressive responses along principal material directions L, T, and S. Panels (a, c, e) show the equivalent stress-equivalent strain curves as a function of grain size and texture under different loading orientations. Panels (b, d, f) collate the corresponding initial yield stresses in the form of Hall-Petch plots.

K (the weakest of the three textures). Solely based on this comparison, one may posit that at this fine grain size the extension twinning is much less profuse in texture B compared to texture E, and perhaps comparable to that in the case of texture K. Note that the stress-strain responses in T-compression (as well as S-tension) do not lend themselves to such a hypothesis. We elaborate upon these further in Section 3.3.

The trends of the Hall-Petch plots (Fig. 4b, 4d, 4f) denote qualitative features that are similar to those discussed for the tensile loading cases. For instance, under twinning dominated loading (L-, T-compression) the initial yield stress is only weakly dependent on the initial textures at all grain sizes, which is consistent with the observation for S-tension. Further, under S-compression texture B exhibits a stronger grain size effect and it is weaker for weaker initial textures. While this result is qualitatively consistent with the L-tension and T-tension, the larger quantitative differences between different textures under S-compression underscores the effect of loading state on the grain size-texture interaction.

Table 4 summarizes the computed Hall-Petch parameters. Interestingly, k_y for the compressive loading is higher compared to the tensile loading across all textures, but particularly for textures B and E. The predicted range of $k_y \sim$ 243-482 MPa μm$^{1/2}$ compares reasonably with experimental values reported by Jain et al. [25] as of $k_y = 472$ MPa μm$^{1/2}$ for AZ31 compressed uniaxially along the rolling (L) direction while the simulations predict it to be $\sim$ 380-407 MPa μm$^{1/2}$.

Table 4 The effective Hall-Petch parameters for the polycrystal Mg alloy AZ31 sample under uniaxial **compression** with respect to material texture and loading direction.

	B $[10°, 15°, 0°]$			E $[30°, 20°, 0°]$			K $[45°, 75°, 45°]$		
	L	T	S	L	T	S	L	T	S
k_y (MPa μm$^{1/2}$)	407.9	362.3	482.3	381.0	333.5	359.9	320.2	271.2	243.1
σ_0 (MPa)	44	36	130	43	37	105	52	50	57

3.3 Interaction of grain size and texture on micromechanical characteristics

To understand the micromechanics underpinnings of the foregoing macroscopic behaviors, we define the volume-averaged relative activity of each deformation mechanism as:

$$\bar{\zeta}^i = \frac{\frac{1}{V}\int \Delta\gamma^i \, \mathrm{d}V}{\frac{1}{V}\int \sum_{j=1}^{N_s+N_{tw}} \Delta\gamma^j \, \mathrm{d}V} \tag{14}$$

where $\Delta\gamma^i$ is the average incremental shear strain due to deformation activity on the particular family of the slip or twinning system i. The denominator represents the total incremental shear strain on all deformation systems averaged over the RVE volume V, and $\mathrm{d}V$ denotes the Gauss point volume.

Fig. 5 and 6 summarize the dependence of the various deformation activities at fixed nominal strain levels ($\bar{\varepsilon}_{\mathrm{eq}} = 0.03$ and 0.10, respectively) as a function of the {0001} pole intensity representing the three textures (cf. Fig. 2) for two limiting cases, i.e. the base material (coarse-grained) and $\bar{d}_{\mathrm{eq}} = 1.8\mu$m (fine-grained). Their corresponding evolution as a function of strain is shown in Appendix A.

3.3.1 Micromechanics under uniaxial tension

As expected, at early stages of deformation, L- and T-tension are governed by slip (Fig. 5a, 5b) while S-tension (Fig. 5c) is governed by extension twinning.

In L- and T-tension, weaker textures exhibit a richer deformation activity than stronger texture in both, the base material and the fine-grained material. This explains the larger difference in the grain size dependent yield stress in T-tension compared to L-tension arising from textural variations (cf. Fig. 3). The differences in the activity landscape of these two slip-dominated tensile responses is noteworthy, which highlights the orientation dependence of the deformation activity for a given combination of grain size and texture, as explained further. Under L-tension (Fig. 5a), prismatic $\langle a \rangle$ slip activity is the primary mechanism in stronger textures over the grain size range and it is more dominant in the fine-grained material. While pyramidal $\langle c+a \rangle$ slip and pyramidal $\langle a \rangle$ slip activities serve as secondary mechanisms in the base material, they are largely

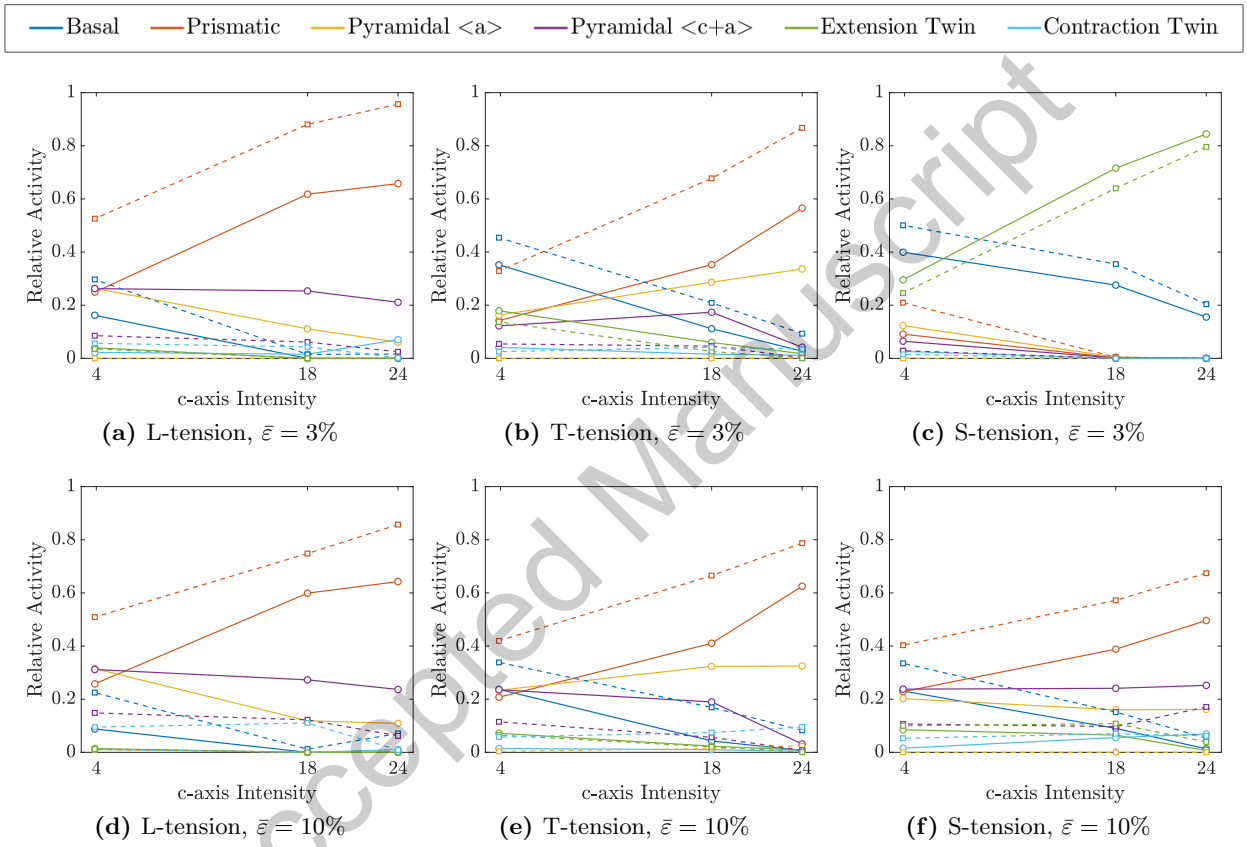

(a) L-tension, $\bar{\varepsilon} = 3\%$ **(b)** T-tension, $\bar{\varepsilon} = 3\%$ **(c)** S-tension, $\bar{\varepsilon} = 3\%$

(d) L-tension, $\bar{\varepsilon} = 10\%$ **(e)** T-tension, $\bar{\varepsilon} = 10\%$ **(f)** S-tension, $\bar{\varepsilon} = 10\%$

Figure 5 Relative activity trends under uniaxial tension at (a-c) $\bar{\varepsilon}_{\text{eq}} = 0.03$ and (d-f) $\bar{\varepsilon}_{\text{eq}} = 0.10$ as a function of {0001} pole intensity. Solid and dashed lines show the trends for the base material and $\bar{d} = 1.8$ μm, respectively. Three textures, B, E, and K are shown on the x-axis with the c-axis intensity (cf. Fig. 2) as an indicator for each texture.

suppressed in the fine-grained material. For the weak texture, the base material response shows that the plastically hard prismatic $\langle a \rangle$ slip, pyramidal $\langle c+a \rangle$ slip, and soft basal $\langle a \rangle$ slip modes are as important as prismatic $\langle a \rangle$ slip; however, with grain refinement the hard mechanisms are dramatically suppressed while the basal $\langle a \rangle$ slip mode plays a secondary role behind the dominant prismatic $\langle a \rangle$ slip. Under T-tension (Fig. 5b), the base material with a weaker texture shows basal $\langle a \rangle$ slip as a preferred mechanism that is further enhanced by grain refinement. Prismatic $\langle a \rangle$ slip, which is a secondary mechanism (with pyramidal $\langle a \rangle$ slip, pyramidal $\langle c+a \rangle$ slip, and ET as tertiary mechanisms) in the base material, becomes more prominent in the fine-grained material in lieu of the tertiary mechanisms. For the strong texture, prismatic $\langle a \rangle$ slip is the governing mechanism that is further strengthened by grain refinement. Seen differently, for these slip-dominated loading states the slip activity landscape is more diverse for weaker textures, particularly in T-tension.

Under S-tension (Fig. 5c), in both the base material and the fine-grained material the stronger the texture the more dominant the extension twinning, albeit the fine-grained material exhibits a somewhat lower activity. The basal $\langle a \rangle$ slip operates as a complementary mechanism in strong textures but serves a primary mechanism for the weak texture in both cases. In fact, in the fine-grained material with a weak texture extension twinning is secondary and is supplemented by the plastically harder prismatic $\langle a \rangle$ slip mode, which explains its weak sensitivity to the yield stress (cf. Fig. 3f) is comparable to the stronger textures despite the prevalence of the soft basal $\langle a \rangle$ slip. With increasing textural strength the importance of prismatic $\langle a \rangle$ slip and other tertiary mechanisms rapidly diminishes and only the basal $\langle a \rangle$ slip remains persistent secondary mechanism. The persistence of basal slip activity highlights the role of texture relative to a limiting single crystal scenario loaded uniaxially along the prismatic axis where no basal slip is activated [62]. For weak textures, the extension twinning activity drops by nearly 60%, and serves only as a secondary mechanism. It is further tempered with grain size reduction. Grain size refinement couples into the weak texture to enhance the pyramidal $\langle c+a \rangle$ activity. At moderate strains ($0.06 \lesssim \varepsilon_{eq} \lesssim 0.10$), all deformation modes are present (in both, large- and fine-grained materials), which is distinct from the activity landscape for texture B where the prismatic slip dominates the flow stress in that regime.

At a larger strain level, the slip-dominated behaviors in L- and T-tension (Fig. 5d, 5e)

continue the same trend as their respective early stage deformation landscape; in contrast, S-tension response is now modified as a result of twinning-induced grain reorientation, Fig. 5f. In effect, it qualitatively reflects the landscape that is similar its slip-dominated counterparts, suggesting that the twinned grains acquire orientations that selectively sample the mechanisms in both L- and T-tension. For instance, while its trend for the prismatic $\langle a \rangle$ slip activity resembles that of T-tension, the pyramidal $\langle c+a \rangle$ slip and pyramidal $\langle a \rangle$ slip activity trends are closer to that of L-tension across the grain size and texture space. Interestingly, in the fine-grained material although the activity of extension twinning is lower (cf. Fig. 5c), the post-twinning prismatic $\langle a \rangle$ slip activity is higher than the base material.

3.3.2 Micromechanics under uniaxial compression

The deformation activity landscape under uniaxial compression is reversed compared to uniaxial tension. L- and T-compression exhibit twinning at early stages (Fig. 6a, 6b) followed by a slip-mediated plasticity post-twinning (Fig. 6d, 6e) while the deformation mechanisms under S-compression (Fig. 6c, 6f) are governed by basal slip (weak texture) or pyramidal $\langle c+a \rangle$ slip (strong texture). Grain size and texture broadly play similar roles in determining the potencies of various individual mechanisms as in tension. In the fine-grained material under L-compression (Fig. 6a), the extension twinning activity is somewhat stronger (and comparable to the base material) across the textural range unlike its counterparts in T-compression (Fig. 6b) and S-tension (Fig. 5c). Further, extension twinning activity for the weak texture (K) drops by nearly 50% relative to the strong texture (B) with a concomitant increase in the basal and prismatic slip activities. The increase in the basal slip activity is similar to that in T-compression and S-tension. At the other end of the spectrum, for the strong texture the basal slip activity is suppressed under L-compression but the prismatic $\langle a \rangle$ slip activity remains an important secondary mechanism, unlike T-compression and S-tension. Although this prismatic $\langle a \rangle$ slip activity persists in the twinning regime, it plays an important role in its macroscopic response, discussed *et seq* (cf. Fig. 8).

At later stages of deformation, the post-twinning ($\varepsilon_{eq} \gtrsim 0.06$) activity landscapes in L and T are rather different. While pyramidal $\langle c+a \rangle$ slip and basal $\langle a \rangle$ slip govern the post-twinning response (at both grain sizes) in L-compression, in T-compression pyramidal $\langle c+a \rangle$ slip becomes increasingly important in stronger textures, although it shows somewhat reduced activity level in

the fine-grained material compared to the base material. This reduction occurs due to increased basal slip activity and, to a lesser extent, pyramidal $\langle a \rangle$ slip and contraction twinning.

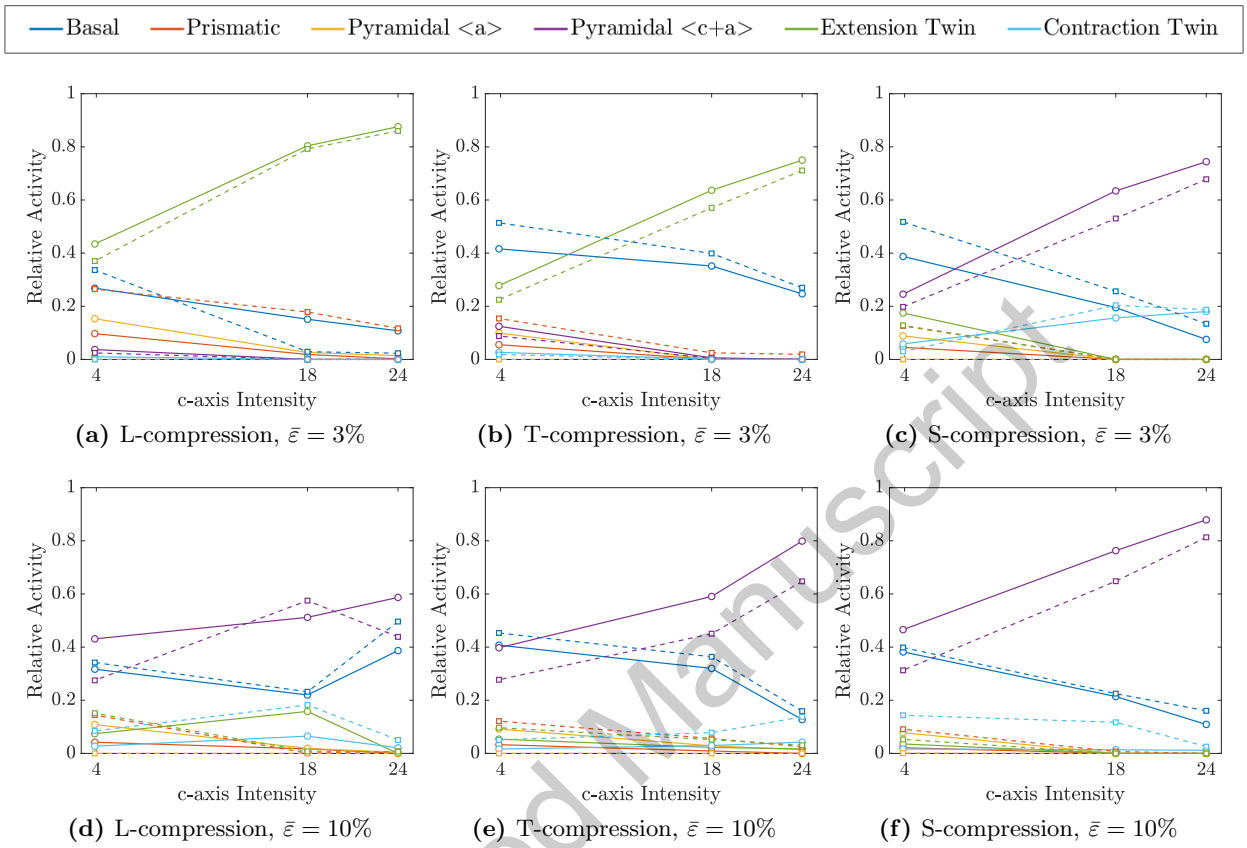

(a) L-compression, $\bar{\varepsilon} = 3\%$ **(b)** T-compression, $\bar{\varepsilon} = 3\%$ **(c)** S-compression, $\bar{\varepsilon} = 3\%$

(d) L-compression, $\bar{\varepsilon} = 10\%$ **(e)** T-compression, $\bar{\varepsilon} = 10\%$ **(f)** S-compression, $\bar{\varepsilon} = 10\%$

Figure 6 Relative activity trends under uniaxial compression at (a-c) $\bar{\varepsilon}_{\text{eq}} = 0.03$ and (d-f) $\bar{\varepsilon}_{\text{eq}} = 0.10$ as a function of {0001} pole intensity. Solid and dashed lines show the trends for the base material and $\bar{d} = 1.8$ μm, respectively. Three textures, B, E, and K are shown on the x-axis with the c-axis intensity (cf. Fig. 2) as an indicator for each texture.

Discussion

4.1 Key mechanisms

The preceding results provide a detailed insight into the different deformation mechanisms that govern the texture-grain size interaction under uniaxial tensile and compressive loading. To facilitate microstructure-property linkages, it is useful to map the deformation activity and texture effect on the flow stresses, σ_{f}, as a function of grain size. For this, we consider two limiting cases of microstructures (textures: B and K, and grain sizes: $\bar{d} = 180\mu$ m (coarse-grained) and $\bar{d} = 1.8\mu$m (fine-grained)) and define the ratio $\bar{\sigma}_{\text{f}} = \sigma_{\text{f}}^{\text{B}}/\sigma_{\text{f}}^{\text{K}}$ for a particular $\bar{d}$.

Broadly, slip-dominated conditions (e.g. L-tension, T-tension, S-compression) result in relative strengthening ($\bar{\sigma}_{\mathrm{f}} > 1$) while twinning-affected scenarios (L-compression, T-compression, S-tension) exhibit relative weakening ($\bar{\sigma}_{\mathrm{f}} < 1$). The interacting effect of texture and grain size is more discernible in twinning affected loading conditions. A closer analysis reveals that variations in Φ play a more important role (compared to φ_1 and φ_2) in determining the twinning contribution to the overall deformation across the grain size regime. As an illustrative example, consider the trends for L-compression. For the strongly textured material, both the coarse-grained and fine-grained responses are dominated by ET with basal slip as the secondary mechanism. In contrast, in the weak texture case the trend differs; for the coarse-grained material, the basal slip and ET are nearly equipotent, while for the fine-grained material the plastically stronger prismatic slip is activated in addition to the basal slip and ET. By way of consequence, the base material exhibits a relative weakening while for the fine-grained material response is more equitable ($\bar{\sigma}_{\mathrm{f}} \approx 1$) thanks to the additional prismatic slip. A similar conclusion can be drawn for the S-tension case. We note that similar trends are also seen under T-direction loading and are omitted here for brevity. *Taken together, under conventional twinning-affected loading states, grain refinement may effectively compensate for textural weakening.*

4.2 Grain size effect on extension twinning

While the relative activity plots indicate a reduced extension twinning activity with grain refinement (save the L-compression case), it needs to be ascertained if that equates to lower twin volume fractions. For instance, a lower relative activity of extension twinning in a fine-grained material could simply be because multiple activities may be contributing to the overall deformation. To that end, Fig. 7a and 7b show the volume-averaged twin volume fraction (Eq. $(11)_2$) for two representative loading cases for the strong texture (Texture B) that are twinning dominated. Clearly, the fine-grained material exhibits a reduction in $\bar{f}^{\mathrm{ET}}$. Initially, $\bar{f}^{\mathrm{ET}}$ increases; it reaches a peak value, and then decreases as the criterion for twinning reorientation $f = f_{\mathrm{cr}}$ is satisfied at increasingly more regions of the polycrystal. These reoriented regions form new sub-grains that further deform via slip and/or twinning. Thus, while the increasing path of $\bar{f}$ indicates the rate at which twinning volume fraction is accrued, the decreasing path depicts the rate at which regions reorient.

Compared to the base material, in the fine-grained material the accumulation of extension

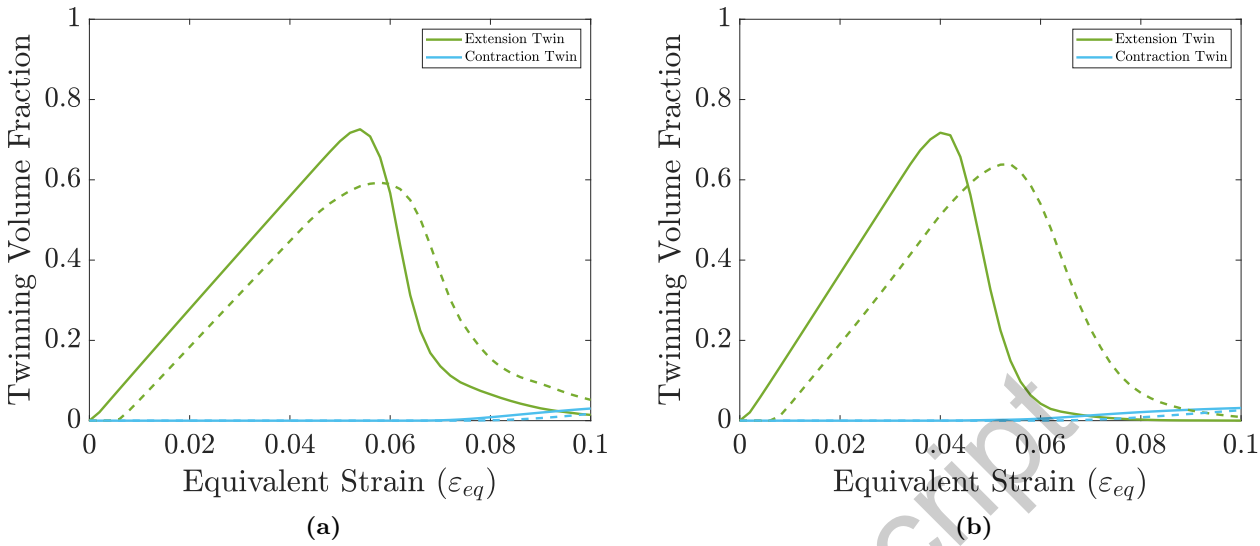

Figure 7 Effect of grain size on twin volume fraction under (a) S-tension and (b) L-compression. The results are for texture B. Solid lines are for the base material and dashed lines are for $\bar{d} = 1.8$ μm.

twinning: (i) occurs at a slower rate underscored by the slower rise of $\bar{f}^{\mathrm{ET}}$, and (ii) results in a lower overall twinned volume over the same strain range asserted by the lower peak $\bar{f}^{\mathrm{ET}}$ in the fine-grained material is lower (by nearly 25%) and the slower decrease after reaching the peak. This observation is particularly interesting given that $k_\tau^{\mathrm{ET}} < k_\tau^{\mathrm{non-basal}}$, cf. Table 2. Several experimental reports exist, which indicate that decreasing grain size decreases the propensity of Mg alloys to extension twinning [25, 41–43]. A putative argument is that k_y for extension twinning is larger than its counterpart for the non-basal slip [41, 50, 91–94]. Another argument based on discrete dislocation dynamics is that the tempering of twinning is a result of the competition between twin boundary induced strengthening and twin growth induced weakening [48]. Against that backdrop, the present results indicate that the decrease in the propensity to extension twinning may not be driven solely by the crystallographic hardening of twinning from grain boundaries. It may be a consequence of the net interaction between the disparate contributions to different mechanisms from the grain size. This assessment is supported by the fact that in Table 3 the effective k_y for texture B under S-tension (twinning dominated) is smaller than its counterparts under L- and T-tension (slip dominated).

The L-compression case is particularly interesting because it shows that while the relative activity of twinning in the fine-grained material is comparable to the base material (cf. Fig. 6a), it

does not imply same level of twin volume fraction. Note that in both cases, the contraction twin volume fraction is small and it decreases with decreasing grain size.

The effect of these micromechanical characteristics on the macroscopic stress-strain evolution is worth noting. Fig. 8 collates the stress-strain curves of the fine-grained material for a particular texture under three twinning-dominated loading states. Note that in the regime $0.06 \leq \varepsilon_{eq} \leq 0.1$, the increase in the flow stress for S-tension and L-compression is 250 MPa and 95 MPa, respectively. This significant difference arises due to the difference in the flow stresses at $\varepsilon_{eq} = 0.06$, which corresponds to the peak twin volume fraction. In S-tension, the flow stress at this strain is ~ 350 MPa, which is much lower than in the case of L-compression (~ 480 MPa). In other words, beyond yield the fine-grained material hardens much more rapidly until $\varepsilon_{eq} = 0.06$ in L-compression than in S-tension. Referring to the relative activity plots (cf. Fig 6a and 5c, also see Fig. A-1g and A-2a), the fundamental difference over that range of deformation is the presence of non-negligible prismatic $\langle a \rangle$ slip and the corresponding absence of the basal $\langle a \rangle$ slip activity in L-compression compared to S-tension. In effect, the activation of prismatic $\langle a \rangle$ slip causes an enhanced hardening during the twinning regime ($0 \lesssim \varepsilon_{eq} \lesssim 0.06$). The net effect of this extra hardening is the diminished sigmoidal nature in the macroscopic stress-strain response under L-compression. On the other hand, the nearly same level of the flow stress (~ 600 MPa) at $\varepsilon_{eq} = 0.1$ in both cases indicates that the details of the deformation activity after twinning do not play a distinctive role. We note in passing that response for T-compression (605-480 = 125 MPa) lies between the S-tension and L-compression, and the corresponding micromechanical activity is consistent with this intermediate behavior.

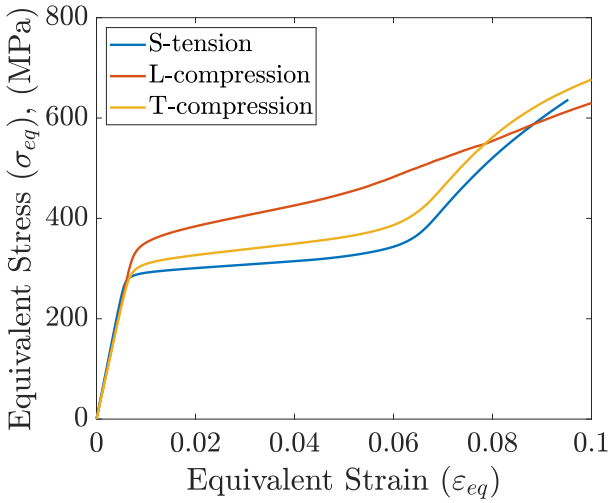

Figure 8 Loading orientation effect in flow stress evolution of twinning-dominated responses for a particular texture (B) and grain size ($\bar{d} = 1.8$ μm).

Fig. 9 collates the role of texture on the overall extension twin volume fraction as a function of grain size for two loading states that generally favor extension twinning. At $\varepsilon_{eq} \sim 0.015$, the grain size effect on the twin volume fraction depends on texture and loading condition, Fig. 9a. For a given texture, the average twin volume fraction increases mildly with increasing grain size. For a given grain size, the strong texture (B) accumulates the largest twin volume fraction and weaker textures show progressively lower amount of twinning. For the intermediate texture (E), which mimics typical experimental rolled textures the twin volume fraction corroborate reasonably with experiments [32]. Moreover, the results indicate that the maximum average extension twin volume fraction (Fig. 9b) is rather insensitive to grain size, but is strongly influenced by texture.

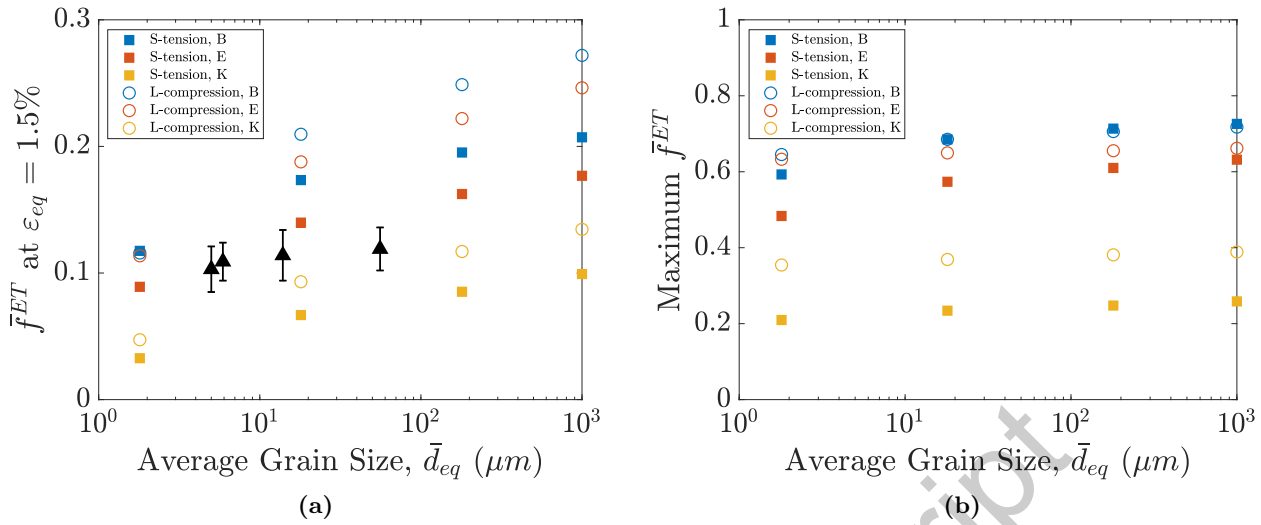

Figure 9 Grain size effect on average extension twin volume fraction $\bar{f}^{\mathrm{ET}}$ for three textures. Panel (a) shows the trends at a nominal strain $\bar{\varepsilon}_{\mathrm{eq}} \sim 0.015$. The experimental data with error bars are from [32]. Panel (b) shows the peak values of $\bar{f}_{\mathrm{ET}}$.

It is useful to estimate the grain size effect on twin statistics, particularly the average number of twins ($\bar{n}_{\mathrm{t}}$) and average twin thickness ($\bar{t}_{\mathrm{t}}$) per grain. The relationship between $\bar{f}, \bar{n}_{\mathrm{t}}$ and $\bar{t}_{\mathrm{t}}$ can be calculated as:

$$\bar{n}_{\mathrm{t}} = \bar{f}\left(\frac{\bar{d}}{\bar{t}_{\mathrm{t}}}\right) \tag{15}$$

In Mg [32, 44], $\bar{t}_{\mathrm{t}}$ appears to depend weakly on the grain size; here, we assume it to be constant $\bar{t}_{\mathrm{t}} \approx 2$ μm over the range of grain sizes considered, which is consistent with Ref. [32]. Across the range of textures and loading orientations, the average number of twins per grain ($\bar{n}_{\mathrm{t}}$) at a nominal strain of 0.015 (cf. Fig. 9a) is 0.084 ± 0.042 ($\bar{d} = 1.8$ μm), 1.43 ± 0.54 ($\bar{d} = 18$ μm), and 17.9 ± 6.21 ($\bar{d} = 180$ μm). The corresponding values at peak twin volume fractions (Fig. 9b) are 0.486 ± 0.15 ($\bar{d} = 1.8$ μm), 5.13 ± 1.49 ($\bar{d} = 18$ μm), and 52.5 ± 14.5 ($\bar{d} = 180$ μm). While these estimates are somewhat lower than those in [32], they are closer to those in Ref. [44].

4.3 Effect on net macroscopic plastic anisotropy and strength asymmetry

Fig. 10 consolidates the grain size and texture effect on the yield stress anisotropy and tension-compression asymmetry. For a given texture, the yield stress in each direction and for each grain size is normalized with respect to the tensile yield stress of the base material along the L-direction. For a given grain size (denoted by a particular color), the shape of the triangle describes the plastic

anisotropy along the three principal directions. An isotropic response manifests as an equilateral triangle and therefore, the more distorted the triangle the more anisotropic the response. The tension-compression asymmetry along a given direction is described by the relative difference in the vertex positions of the solid (tensile) and dashed (compressive) triangles, which manifests as a relative shift between the solid and dashed triangles of a given color (cf. Fig. 10). Comparing Fig. 10a-10c, it can be inferred that textural weakening and grain refinement create synergistic effect toward reducing the plastic anisotropy and tension-compression asymmetry. For example, for the weakest texture (K, cf. Fig. 10c), the tension-compression asymmetry is negligible along the three principal directions; moreover, the plastic anisotropy (in both, tension and compression) is somewhat tempered compared to its coarse-grained counterparts. For the strong (B) texture, the tensile responses are relatively less anisotropic for the fine-grained material (green) compared to their corresponding coarse-grained counterparts (orange and blue). While the plastic anisotropy in compression does decrease, the effect is not as significant as in tension. By way of consequence, the effect of grain size refinement on the tension-compression asymmetry now depends on the loading direction. For L and T directions, the grain size refinement tends to reduce tension-compression asymmetry while the effect is relatively weak for the S-direction. As expected, the trends for texture E are intermediate to textures B and K.

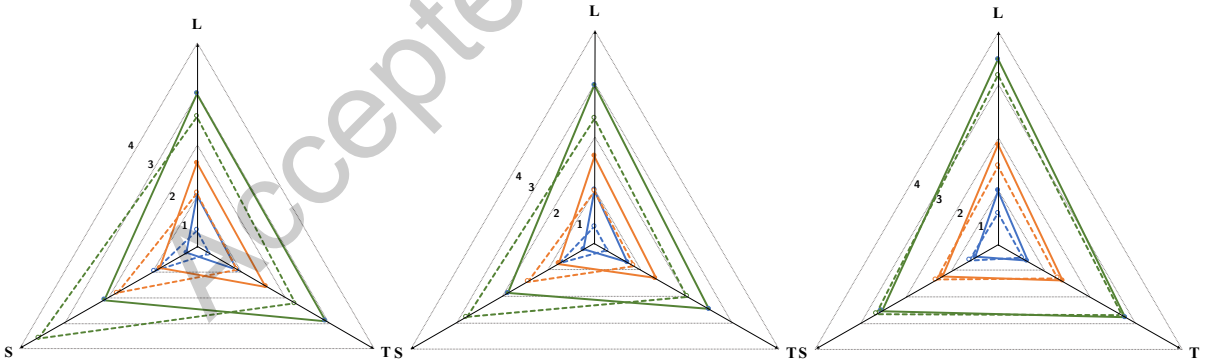

(a) Texture B **(b)** Texture E **(c)** Texture K

Figure 10 Radar plots indicating the normalized macroscopic yield stress anisotropy and tension-compression asymmetry for the Base material (blue), $\bar{d} = 18\mu$m (orange), and $\bar{d} = 1.8\mu$m (green). Solid lines denote tensile responses and dashed lines denote compressive responses. For each texture, the yield stress in each direction and for each grain size is normalized with reference to the corresponding tensile yield stress of the base material along the L-direction. The light gray lines are normalized iso-strength contours and the corresponding numbers denote the normalized strength value.

4.4 Potential implications on damage

Given the intrinsic crystallographic plastic anisotropy and tension-compression asymmetry, a thornier challenge is to assess the role of grain size in the damage tolerance in Mg alloys. While experiments suggest that grain size refinement may improve room-temperature ductility posited to the reduction of extension twinning [23, 90, 95], a ubiquitous increase in uniaxial tensile ductility may not always be possible given the intricate dependencies on texture and loading orientation [31]. To that end, the interplay between texture and grain size on damage micromechanics remains relatively unexplored [11]. In coarse-grained polycrystals [44] as well as in single crystals [96], extension twinning has been argued to either promote toughening or cause premature cracking [97–101]. In fine-grained microstructures, a reduced propensity to twinning has been posited to decelerate void growth, although in the process it may activate an alternate failure mode, e.g. shear instability [10, 11]. Nevertheless, others report improved tensile ductility in the presence rather than the absence of extension twinning in fine-grained Mg alloys [31]. These insightful observations hint at potentially more complex interactions between deformation mechanisms and damage than currently appreciated.

Using a rational basis rooted in the micromechanics of anisotropic plasticity [102] and tension-compression asymmetry [103], the role of texture in the damage tolerance of Mg alloys can be assessed [104–108]. High-resolution single crystal simulations of void growth [62] reveal delayed porosity evolution due to the activation of multiple extension twin variants around the void. Concurrently, the twin boundary-void surface interactions result in complex void shapes, which may cause void sharpening. While these modeling paradigms do not consider grain size effect, they inform how the different mechanisms and the resulting net plastic anisotropy influence damage evolution. For instance, as suggested in our recent work [108], for a material with a prescribed crystallographic anisotropy there may be a set of textures that offer better damage tolerance compared to other textures, which relates to the net plastic anisotropy. Such information may provide a glimpse of the potential role of grain size and texture in the damage occurrence. In that regard, the broader trends in Fig. 10 may offer some direction. The synergistic effect of grain size refinement and weakening of textures in tempering the net plastic anisotropy, and the tension-compression asymmetry could be beneficial in improving the damage tolerance of Mg

alloys while retaining or improving the strength. From a modeling perspective, the reduced tension-compression asymmetry could permit the use of established anisotropic porous plasticity models in damage prediction, although responses and trends along other (off-axis) directions are necessary to establish the full landscape of the texture and grain size effects on the stress and deformation anisotropy.

Summary

This work presents a computational investigation of the interacting effects between the grain size, texture, and loading orientation on the macroscopic responses of Mg alloys. Using a single crystal plasticity framework endowed with size-dependent activation thresholds and hardening of crystallographic slip and twinning mechanisms, resolved polycrystalline microstructures are modeled to account for the effect of grain size on the tensile and compressive behaviors along principal material directions. Three textures spanning a wide range of textural strengths –from very strong to very weak– are considered. The salient observations are summarized below:

1. The grain size strengthening couples into textural effects in a complicated manner. Yet, these two microstructural features play a synergistic role in reducing the net plastic anisotropy and tension-compression asymmetry.

2. For a given loading state (tension or compression), the Hall-Petch effect embedded at the crystallographic scale is retrieved in the macroscopic yield stress. On the other hand, the macroscopic flow stress deviates somewhat with the exponent ranging between -0.42 and -0.64.

3. In tension, the Hall-Petch slope is mildly dependent on the loading direction (for a given texture) but exhibits a stronger dependence on the texture. For a given loading direction, it is smaller for weaker textures. In compression, the effect of loading direction on the Hall-Petch slope is comparable to the texture effect. From a mechanisms perspective, the textural variability effect on the Hall-Petch slope appears to be stronger for slip-dominated loading states than twinning-dominated states.

4. Extension twinning is indeed tempered with grain size refinement and this effect pervades

textures as well as loading orientations. Importantly, the grain size dependent crystallographic hardening of twinning CRSS ~~does not need to~~ be higher than that of slip for this emergent characteristic.

5. The lack of characteristic sigmoidal hardening in a twinning-affected macroscopic stress-strain response may not imply lack of twinning. Instead, net interactions between disparate deformation mechanisms modulated by reduced grain size ~~may manifest into a similar qualitative~~ macroscopic stress-strain behavior.

These observations provide deeper insight into the complex emergent interactions brought about by the coupling between initial microstructural states and loading. They potentially offer guidelines toward designing damage-tolerant microstructures.

Acknowledgements

SPJ acknowledges support provided by the National Science Foundation under Grant Number CMMI-1932976. Support for BR was provided by the Army Research Laboratory and was accomplished under Cooperative Agreement Number W911NF-12-2-0022. The views and conclusions contained in this document are those of the authors and should not be interpreted as representing the official policies, either expressed or implied, of the Army Research Laboratory or the U.S. Government. The U.S. Government is authorized to reproduce and distribute reprints for Government purposes notwithstanding any copyright notation herein. The authors would like to acknowledge Dr. Jeffrey T. Lloyd (ARL) for helpful discussions and the reviewers for their constructive comments. The authors also acknowledge the use of the Opuntia Cluster and the advanced support from the Research Computing Data Core at the University of Houston to carry out the research presented here.

Appendix: Relative activity details

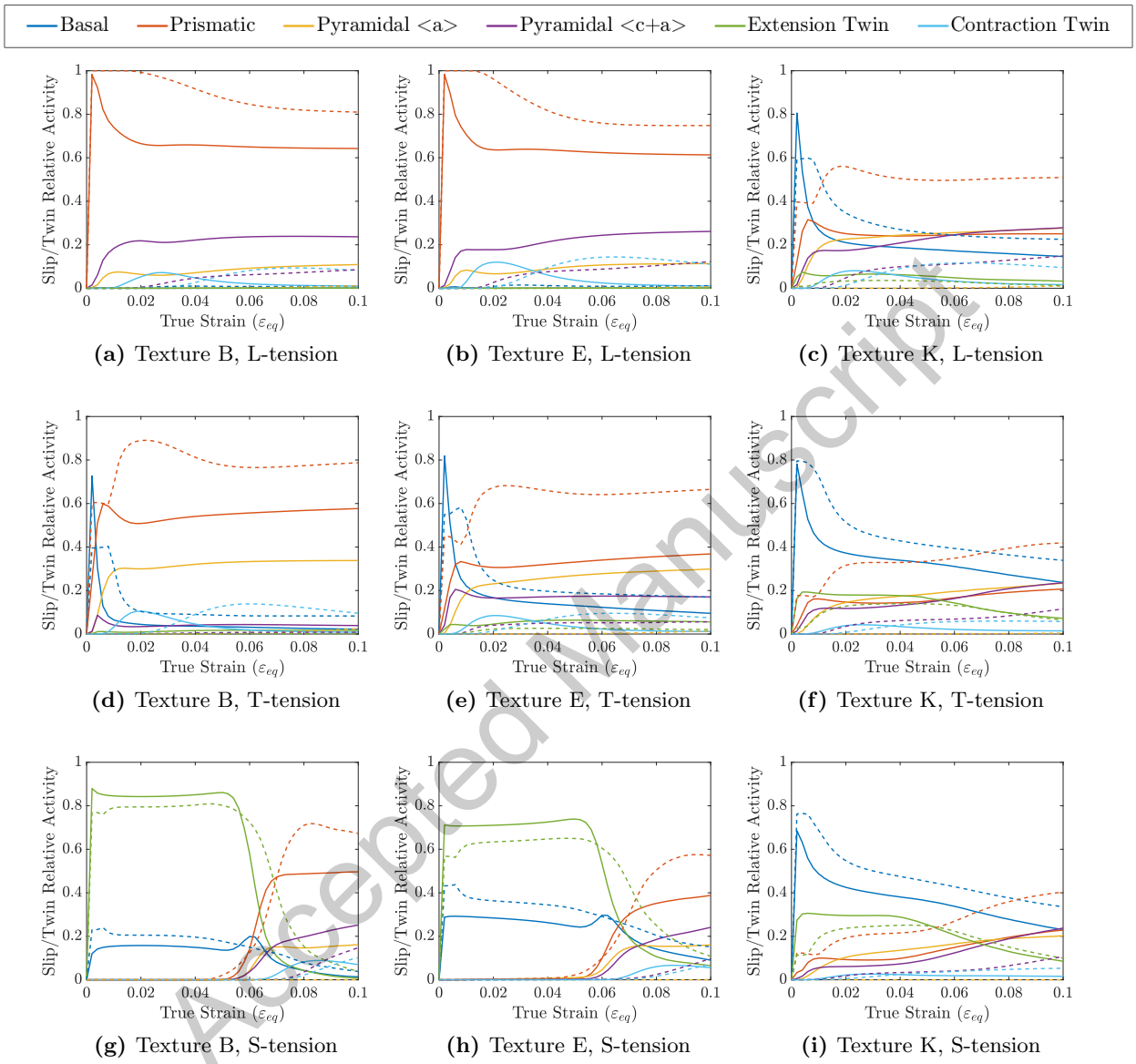

(a) Texture B, L-tension **(b)** Texture E, L-tension **(c)** Texture K, L-tension

(d) Texture B, T-tension **(e)** Texture E, T-tension **(f)** Texture K, T-tension

(g) Texture B, S-tension **(h)** Texture E, S-tension **(i)** Texture K, S-tension

Figure A-1 Effect of grain size and texture on the evolution of relative deformation activities under uniaxial tension. Panels (a-c) L-tension, (d-f) T-tension, and (g-i) S-tension. Solid lines represent the base material and dashed lines represent $\bar{d} = 1.8$ μm.

References

[1] B.L Mordike and T Ebert. Magnesium: Properties — applications — potential. Materials Science and Engineering: A, 302(1):37–45, 2001. ISSN 0921-5093. doi: 10.1016/

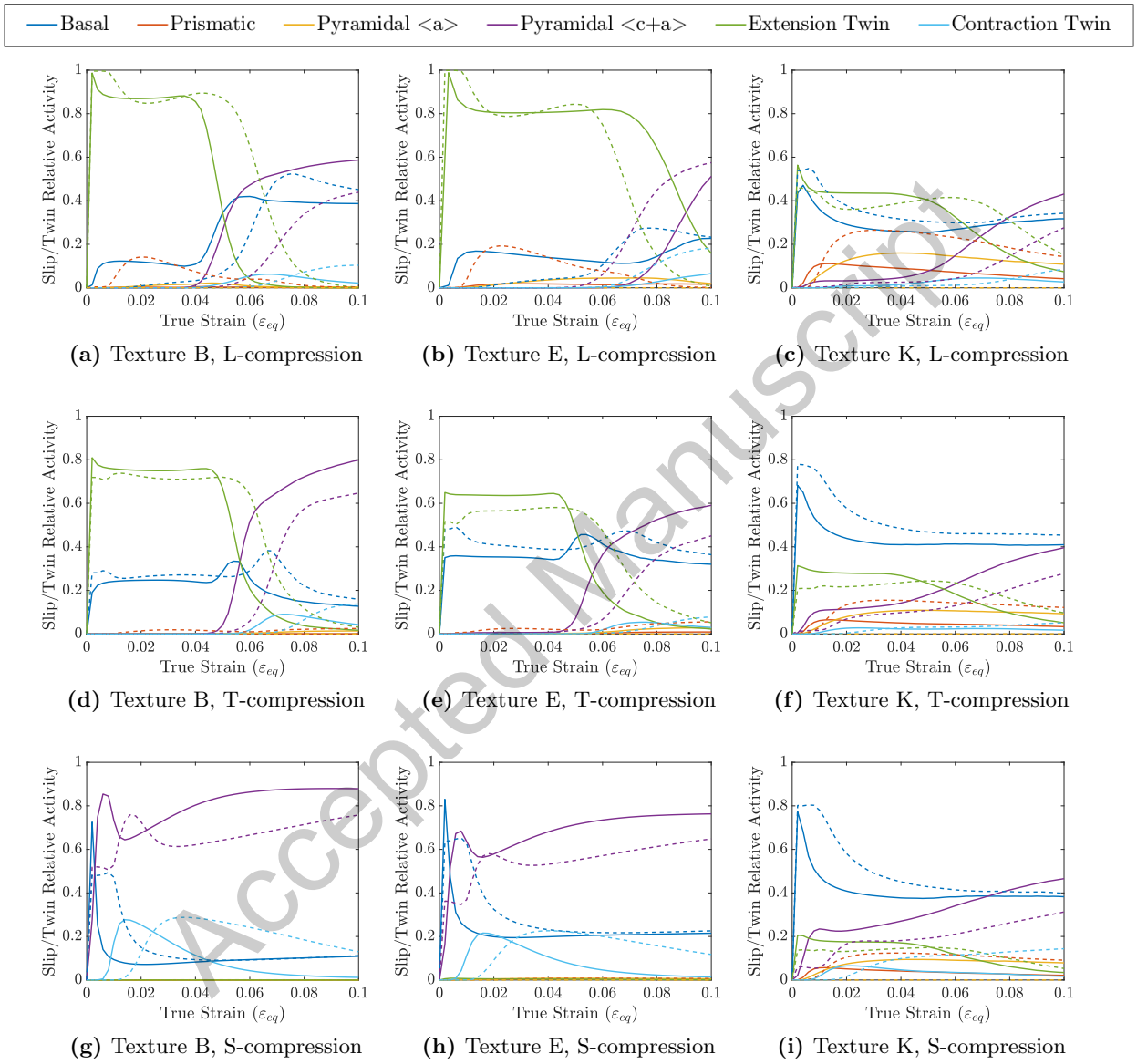

(a) Texture B, L-compression **(b)** Texture E, L-compression **(c)** Texture K, L-compression

(d) Texture B, T-compression **(e)** Texture E, T-compression **(f)** Texture K, T-compression

(g) Texture B, S-compression **(h)** Texture E, S-compression **(i)** Texture K, S-compression

Figure A-2 Effect of grain size and texture on the evolution of relative deformation activities under uniaxial compression. Panels (a-c) L-compression, (d-f) T-compression, and (g-i) S-compression. Solid lines represent the base material and dashed lines represent $\bar{d} = 1.8$ μm.

S0921-5093(00)01351-4. URL http://www.sciencedirect.com/science/article/pii/S0921509300013514.

[2] H Friedrich and S Schumann. Research for a "new age of magnesium" in the automotive industry. Journal of Materials Processing Technology, 117(3):276–281, 2001. ISSN 0924-0136. doi: 10.1016/S0924-0136(01)00780-4. URL http://www.sciencedirect.com/science/article/pii/S0924013601007804.

[3] Mark Easton, Aiden Beer, Matthew Barnett, Chris Davies, Gordon Dunlop, Yvonne Durandet, Stuart Blacket, Tim Hilditch, and Peter Beggs. Magnesium alloy applications in automotive structures. JOM, 60(11):57, 2008.

[4] Erlin Zhang, Dongsong Yin, Liping Xu, Lei Yang, and Ke Yang. Microstructure, mechanical and corrosion properties and biocompatibility of Mg—Zn—Mn alloys for biomedical application. Materials Science and Engineering: C, 29(3):987–993, 2009. ISSN 0928-4931. doi: 10.1016/j.msec.2008.08.024. URL http://www.sciencedirect.com/science/article/pii/S0928493108002117.

[5] Zhong Yang, JP Li, JX Zhang, GW Lorimer, and JAMSEL Robson. Review on research and development of magnesium alloys. Acta Metallurgica Sinica (english Letters), 21(5):313–328, 2009.

[6] G Sambasiva Rao and YVRK Prasad. Grain boundary strengthening in strongly textured magnesium produced by hot rolling. Metallurgical Transactions A, 13(12):2219–2226, 1982.

[7] W Yuan, SK Panigrahi, J-Q Su, and RS Mishra. Influence of grain size and texture on hall–petch relationship for a magnesium alloy. Scripta Materialia, 65(11):994–997, 2011.

[8] Qingda Yang and AK Ghosh. Deformation behavior of ultrafine-grain (ufg) az31b mg alloy at room temperature. Acta Materialia, 54(19):5159–5170, 2006.

[9] Ruixiao Zheng, Jun-Ping Du, Si Gao, Hidetoshi Somekawa, Shigenobu Ogata, and Nobuhiro Tsuji. Transition of dominant deformation mode in bulk polycrystalline pure mg by ultra-grain refinement down to sub-micrometer. Acta Materialia, 2020.

[10] SH Mohamadi Azghandi, M Weiss, BD Arhatari, and MR Barnett. Grain size and void formation in mg alloy az31. Journal of Alloys and Compounds, 816:152618, 2020.

[11] S.H. Mohamadi Azghandi, M. Weiss, B.D. Arhatari, J. Adrien, E. Maire, and M.R. Barnett. A rationale for the influence of grain size on failure of magnesium alloy az31: an in situ x-ray microtomography study. Acta Materialia, 2020. doi: 10.1016/j.actamat.2020.09.016.

[12] Jian-Feng Nie. Precipitation and hardening in magnesium alloys. Metallurgical and Materials Transactions A, 43(11):3891–3939, 2012.

[13] Jian Feng Nie, YM Zhu, JZ Liu, and Xi-Ya Fang. Periodic segregation of solute atoms in fully coherent twin boundaries. Science, 340(6135):957–960, 2013.

[14] Hucheng Pan, Yuping Ren, He Fu, Hong Zhao, Liqing Wang, Xiangying Meng, and Gaowu Qin. Recent developments in rare-earth free wrought magnesium alloys having high strength: A review. Journal of Alloys and Compounds, 663:321–331, 2016.

[15] Nicole Stanford, Jie Geng, Young Bum Chun, Chris Huw John Davies, Jian Feng Nie, and Matthew Robert Barnett. Effect of plate-shaped particle distributions on the deformation behaviour of magnesium alloy az91 in tension and compression. Acta Materialia, 60(1):218–228, 2012.

[16] Joseph D Robson and Matthew R Barnett. The effect of precipitates on twinning in magnesium alloys. Advanced Engineering Materials, 21(4):1800460, 2019.

[17] H Ferkel and BL Mordike. Magnesium strengthened by sic nanoparticles. Materials Science and Engineering: A, 298(1-2):193–199, 2001.

[18] Lian-Yi Chen, Jia-Quan Xu, Hongseok Choi, Marta Pozuelo, Xiaolong Ma, Sanjit Bhowmick, Jenn-Ming Yang, Suveen Mathaudhu, and Xiao-Chun Li. Processing and properties of magnesium containing a dense uniform dispersion of nanoparticles. Nature, 528(7583):539–543, 2015.

[19] Meisam K Habibi, Shailendra P Joshi, and Manoj Gupta. Hierarchical magnesium nanocomposites for enhanced mechanical response. Acta Materialia, 58(18):6104–6114, 2010.

[20] E O Hall. The Deformation and Ageing of Mild Steel: III Discussion of Results. Proceedings of the Physical Society. Section B, 64(9):747, September 1951. ISSN 0370-1301. doi: 10.1088/0370-1301/64/9/303.

[21] NJ Petch. The cleavage strength of polycrystals. Journal of the Iron and Steel Institute, 174: 25—-28, 1953.

[22] HJ Choi, Y Kim, JH Shin, and DongHyun Bae. Deformation behavior of magnesium in the grain size spectrum from nano-to micrometer. Materials Science and Engineering: A, 527(6): 1565–1570, 2010.

[23] SM Razavi, DC Foley, I Karaman, KT Hartwig, O Duygulu, LJ Kecskes, SN Mathaudhu, and VH Hammond. Effect of grain size on prismatic slip in mg–3al–1zn alloy. Scripta Materialia, 67(5):439–442, 2012.

[24] Y.N. Wang, C.I. Chang, C.J. Lee, H.K. Lin, and J.C. Huang. Texture and weak grain size dependence in friction stir processed Mg–Al–Zn alloy. Scripta Materialia, 55(7):637–640, October 2006. ISSN 1359-6462. doi: 10.1016/j.scriptamat.2006.06.005. URL https://linkinghub.elsevier.com/retrieve/pii/S1359646206004325.

[25] A. Jain, O. Duygulu, D. W. Brown, C. N. Tomé, and S. R. Agnew. Grain size effects on the tensile properties and deformation mechanisms of a magnesium alloy, AZ31B, sheet. Materials Science and Engineering A, 486(1-2):545–555, July 2008. ISSN 0921-5093. doi: 10.1016/j.msea.2007.09.069.

[26] Meisam K Habibi, Manoj Gupta, and Shailendra P Joshi. Size-effects in textural strengthening of hierarchical magnesium nano-composites. Materials Science and Engineering: A, 556: 855–863, 2012.

[27] Bo Guan, Yunchang Xin, Xiaoxu Huang, Peidong Wu, and Qing Liu. Quantitative prediction of texture effect on Hall–Petch slope for magnesium alloys. Acta Materialia, 173:142–152, July 2019. ISSN 1359-6454. doi: 10.1016/j.actamat.2019.05.016.

[28] Akihiro Yamashita, Zenji Horita, and Terence G. Langdon. Improving the mechanical properties of magnesium and a magnesium alloy through severe plastic deformation. Materials Science and Engineering A, 300(1-2):142–147, February 2001. ISSN 0921-5093. doi: 10.1016/S0921-5093(00)01660-9.

[29] W. J. Kim, S. I. Hong, Y. S. Kim, S. H. Min, H. T. Jeong, and J. D. Lee. Texture development and its effect on mechanical properties of an AZ61 Mg alloy fabricated by equal channel angular pressing. Acta Materialia, 51(11):3293–3307, June 2003. ISSN 1359-6454. doi: 10.1016/S1359-6454(03)00161-7.

[30] H. Y. Chao, Y. Yang, X. Wang, and E. D. Wang. Effect of grain size distribution and texture on the cold extrusion behavior and mechanical properties of AZ31 Mg alloy. Materials Science and Engineering A, 528(9):3428–3434, April 2011. ISSN 0921-5093. doi: 10.1016/j.msea.2011.01.020.

[31] DC Foley, M Al-Maharbi, KT Hartwig, I Karaman, LJ Kecskes, and SN Mathaudhu. Grain refinement vs. crystallographic texture: Mechanical anisotropy in a magnesium alloy. Scripta Materialia, 64(2):193–196, 2011.

[32] Alireza Ghaderi and Matthew R Barnett. Sensitivity of deformation twinning to grain size in titanium and magnesium. Acta Materialia, 59(20):7824–7839, 2011.

[33] Huihui Yu, Yunchang Xin, Maoyin Wang, and Qing Liu. Hall-Petch relationship in Mg alloys: A review. Journal of Materials Science and Technology, 34(2):248–256, February 2018. ISSN 1005-0302. doi: 10.1016/j.jmst.2017.07.022.

[34] I. R. Ahmad and D. W. Shu. Compressive and constitutive analysis of AZ31B magnesium alloy over a wide range of strain rates. Materials Science and Engineering A, 592:40–49, January 2014. ISSN 0921-5093. doi: 10.1016/j.msea.2013.10.056.

[35] Bin Li, Shailendra P. Joshi, O. Almagri, Q. Ma, K.T. Ramesh, and T. Mukai. Rate-dependent hardening due to twinning in an ultrafine-grained magnesium alloy. Acta Materialia, 60 (4):1818–1826, 2012. ISSN 1359-6454. doi: 10.1016/j.actamat.2011.12.002. URL http://www.sciencedirect.com/science/article/pii/S1359645411008640.

[36] Xiangyu Sun, Yazhou Guo, Qiuming Wei, Yulong Li, and Shuangyin Zhang. A comparative study on the microstructure and mechanical behavior of titanium: Ultrafine grain vs. coarse grain. Materials Science and Engineering: A, 669:226–245, 2016.

[37] Christopher S Meredith, Jeffrey T Lloyd, and Tomoko Sano. The quasi-static and dynamic response of fine-grained Mg alloy AMX602: An experimental and computational study. Materials Science and Engineering: A, 673:73–82, 2016.

[38] J.T. Lloyd, A.J. Matejunas, R. Becker, T.R. Walter, M.W. Priddy, and J. Kimberley. Dynamic tensile failure of rolled magnesium: Simulations and experiments quantifying the role of texture and second–phase particles. International Journal of Plasticity, 114:174–195, 2019. ISSN 0749-6419. doi: 10.1016/j.ijplas.2018.11.002. URL http://www.sciencedirect.com/science/article/pii/S0749641918303243.

[39] B. Q. Shi, Y. Q. Cheng, X. L. Shang, H. Yan, R. S. Chen, and W. Ke. Hall-Petch relationship, twinning responses and their dependences on grain size in the rolled Mg-Zn and Mg-Y alloys. Materials Science and Engineering A, 743:558–566, January 2019. ISSN 0921-5093. doi: 10.1016/j.msea.2018.04.063.

[40] Huihui Yu, Changzheng Li, Yunchang Xin, Adrien Chapuis, Xiaoxu Huang, and Qing Liu. The mechanism for the high dependence of the Hall-Petch slope for twinning/slip on texture in Mg alloys. Acta Materialia, 128:313–326, April 2017. ISSN 1359-6454. doi: 10.1016/j.actamat.2017.02.044.

[41] M. R. Barnett, Z. Keshavarz, A. G. Beer, and D. Atwell. Influence of grain size on the compressive deformation of wrought Mg-3Al-1Zn. Acta Materialia, 52(17):5093–5103, October 2004. ISSN 1359-6454. doi: 10.1016/j.actamat.2004.07.015.

[42] Patrik Dobroň, František Chmelík, Sangbong Yi, Kseniya Parfenenko, Dietmar Letzig, and Jan Bohlen. Grain size effects on deformation twinning in an extruded magnesium alloy tested in compression. Scripta Materialia, 65(5):424–427, September 2011. ISSN 1359-6462. doi: 10.1016/j.scriptamat.2011.05.027.

[43] S. M. Yin, C. H. Wang, Y. D. Diao, S. D. Wu, and S. X. Li. Influence of Grain Size and Texture on the Yield Asymmetry of Mg-3Al-1Zn Alloy. Journal of Materials Science and Technology, 27(1):29–34, January 2011. ISSN 1005-0302. doi: 10.1016/S1005-0302(11)60021-2.

[44] M Arul Kumar and Irene J Beyerlein. Influence of plastic properties on the grain size effect on twinning in ti and mg. Materials Science and Engineering: A, 771:138644, 2020.

[45] Dv Hull. Effect of grain size and temperature on slip, twinning and fracture in 3% silicon iron. Acta metallurgica, 9(3):191–204, 1961.

[46] MA Meyers, O Vöhringer, and VA Lubarda. The onset of twinning in metals: a constitutive description. Acta Materialia, 49(19):4025–4039, 2001.

[47] Jeffrey Townsend Lloyd. Implications of limited slip in crystal plasticity. PhD thesis, Georgia Institute of Technology, 2010.

[48] Haidong Fan, Sylvie Aubry, Athanasios Arsenlis, and Jaafar A El-Awady. Grain size effects on dislocation and twinning mediated plasticity in magnesium. Scripta Materialia, 112:50–53, 2016.

[49] JT Lloyd. A dislocation-based model for twin growth within and across grains. Proceedings of the Royal Society A: Mathematical, Physical and Engineering Sciences, 474(2210):20170709, 2018.

[50] MR Barnett. A rationale for the strong dependence of mechanical twinning on grain size. Scripta Materialia, 59(7):696–698, 2008.

[51] Yi Wang and Hahn Choo. Influence of texture on Hall-Petch relationships in an Mg alloy. Acta Materialia, 81:83–97, December 2014. ISSN 1359-6454. doi: 10.1016/j.actamat.2014.08.023. URL http://www.sciencedirect.com/science/article/pii/S1359645414006247.

[52] Joseph D Robson, N Stanford, and Matthew Robert Barnett. Effect of precipitate shape on slip and twinning in magnesium alloys. Acta Materialia, 59(5):1945–1956, 2011.

[53] Ronald W Armstrong. Dislocation pile-ups, material strength levels, and thermal activation. Metallurgical and Materials Transactions A, 47(12):5801–5810, 2016.

[54] A. Jain and S. R. Agnew. Modeling the temperature dependent effect of twinning on the behavior of magnesium alloy AZ31B sheet. Materials Science and Engineering A, 462(1-2): 29–36, July 2007. ISSN 0921-5093. doi: 10.1016/j.msea.2006.03.160.

[55] IJ Beyerlein, RJ McCabe, and CN Tomé. Effect of microstructure on the nucleation of deformation twins in polycrystalline high-purity magnesium: a multi-scale modeling study. Journal of the Mechanics and Physics of Solids, 59(5):988–1003, 2011.

[56] M Arul Kumar, Irene Jane Beyerlein, and Carlos N Tome. Grain size constraints on twin expansion in hexagonal close packed crystals. Journal of Applied Physics, 120(15):155105, 2016.

[57] Morton E. Gurtin, Lallit Anand, and Suvrat P. Lele. Gradient single-crystal plasticity with free energy dependent on dislocation densities. Journal of the Mechanics and Physics of Solids, 55(9):1853–1878, September 2007. ISSN 0022-5096. doi: 10.1016/j.jmps.2007.02.006.

[58] Hsueh Hung Fu, David J. Benson, and Marc André Meyers. Computational description of nanocrystalline deformation based on crystal plasticity. Acta Materialia, 52(15):4413–4425, September 2004. ISSN 1359-6454. doi: 10.1016/j.actamat.2004.05.036.

[59] Jing Zhang and Shailendra P Joshi. Phenomenological crystal plasticity modeling and detailed micromechanical investigations of pure magnesium. Journal of the Mechanics and Physics of Solids, 60(5):945–972, 2012.

[60] Balaji Selvarajou, Joong-Ho Shin, Tae Kwon Ha, In-suk Choi, Shailendra P Joshi, and Heung Nam Han. Orientation-dependent indentation response of magnesium single crystals: modeling and experiments. Acta Materialia, 81:358–376, 2014.

[61] Jing Zhang, Qiuming Wei, and Shailendra P Joshi. Effects of reinforcement morphology on the mechanical behavior of magnesium metal matrix composites based on crystal plasticity modeling. Mechanics of Materials, 95:1–14, 2016.

[62] Balaji Selvarajou, Shailendra P Joshi, and A Amine Benzerga. Void growth and coalescence in hexagonal close packed crystals. Journal of the Mechanics and Physics of Solids, 125: 198–224, 2019.

[63] Balaji Selvarajou, Babak Kondori, A Amine Benzerga, and Shailendra P Joshi. On plastic flow in notched hexagonal close packed single crystals. Journal of the Mechanics and Physics of Solids, 94:273–297, 2016.

[64] Balaji Selvarajou, Shailendra P Joshi, and A Amine Benzerga. Three dimensional simulations of texture and triaxiality effects on the plasticity of magnesium alloys. Acta Materialia, 127: 54–72, 2017.

[65] Shahmeer Baweja, Vijay R Ramesh, Padmeya P Indurkar, and Shailendra P Joshi. A numerical study of strain-rate and triaxiality effects in magnesium alloys. Journal of Dynamic Behavior of Materials, pages 1–13, 2020.

[66] Padmeya P. Indurkar, Shahmeer Baweja, Robert Perez, and Shailendra P. Joshi. Predicting textural variability effects in the anisotropic plasticity and stability of hexagonal metals: Application to magnesium and its alloys. International Journal of Plasticity, page 102762, April 2020. ISSN 0749-6419. doi: 10.1016/j.ijplas.2020.102762.

[67] William F. Hosford. The Mechanics of Crystals and Textured Polycrystals. Oxford University Press, New York, 1993.

[68] Thao Nguyen, D.J. Luscher, and J.W. Wilkerson. A dislocation-based crystal plasticity framework for dynamic ductile failure of single crystals. Journal of the Mechanics and Physics of Solids, 108:1–29, November 201. ISSN 0022-5096. doi: 10.1016/J.JMPS.2017.07.020. URL https://www.sciencedirect.com/science/article/pii/S0022509617301813.

[69] J. W. Wilkerson. On the micromechanics of void dynamics at extreme rates. International Journal of Plasticity, 95:21–42, August 2017. ISSN 0749-6419. doi: 10.1016/j.ijplas.2017.03.008.

[70] Georges Saada and Patrick Veyssière. Chapter 61 Work hardening of face centred cubic crystals. Dislocations intersection and cross slip. Dislocations in Solids, 11(C):413–458, January 2002. ISSN 1572-4859. doi: 10.1016/S1572-4859(02)80012-2.

[71] Jaafar A. El-Awady. Unravelling the physics of size-dependent dislocation-mediated plasticity. Nature Communications, 6(May 2014):1–9, 2015. ISSN 2041-1723. doi: 10.1038/ncomms6926.

[72] A. Acharya and A. J. Beaudoin. Grain-size effect in viscoplastic polycrystals at moderate strains. Journal of the Mechanics and Physics of Solids, 48(10):2213–2230, October 2000. ISSN 0022-5096. doi: 10.1016/S0022-5096(00)00013-2.

[73] T. Narutani and J. Takamura. Grain-size strengthening in terms of dislocation density measured by resistivity. Acta Metallurgica Et Materialia, 39(8):2037–2049, August 1991. ISSN 0956-7151. doi: 10.1016/0956-7151(91)90173-X. URL https://linkinghub.elsevier.com/retrieve/pii/095671519190173X.

[74] N. Hansen. The effect of grain size and strain on the tensile flow stress of aluminium at room temperature. Acta Metallurgica, 25(8):863–869, August 1977. ISSN 0001-6160. doi: 10.1016/0001-6160(77)90171-7.

[75] N. Hansen and B. Ralph. The strain and grain size dependence of the flow stress of copper. Acta Metallurgica, 30(2):411–417, February 1982. ISSN 0001-6160. doi: 10.1016/0001-6160(82)90221-8.

[76] X.Y. Lou, M. Li, R.K. Boger, S.R. Agnew, and R.H. Wagoner. Hardening evolution of AZ31B Mg sheet. International Journal of Plasticity, 23(1):44–86, 2007.

[77] W.B. Hutchinson and M.R. Barnett. Effective values of critical resolved shear stress for slip in polycrystalline magnesium and other HCP metals. Scripta Materialia, 63(7):737–740, 2010. ISSN 1359-6462. doi: 10.1016/j.scriptamat.2010.05.047. URL http://www.sciencedirect.com/science/article/pii/S1359646210003726.

[78] S.R. Agnew, C.N. Tomé, D.W. Brown, T.M. Holden, and S.C. Vogel. Study of slip mechanisms in a magnesium alloy by neutron diffraction and modeling. Scripta Materialia, 48(8):1003–1008, 2003.

[79] Seong-Gu Hong, Sung Hyuk Park, and Chong Soo Lee. Role of $\{10\bar{1}2\}$ twinning characteristics in the deformation behavior of a polycrystalline magnesium alloy. Acta Materialia, 58(18):5873–5885, 2010. ISSN 1359-6454. doi: 10.1016/j.actamat.2010.07.002. URL http://www.sciencedirect.com/science/article/pii/S135964541000426X.

[80] R. Quey, P.R. Dawson, and F. Barbe. Large-scale 3D random polycrystals for the finite element method: Generation, meshing and remeshing. Computer Methods in Applied Mechanics

and Engineering, 200(17):1729–1745, 2011. ISSN 0045-7825. doi: 10.1016/j.cma.2011.01.002. URL http://www.sciencedirect.com/science/article/pii/S004578251100003X.

[81] F Bachmann, Ralf Hielscher, and Helmut Schaeben. Texture analysis with MTEX–free and open source software toolbox. In Solid State Phenomena, volume 160, pages 63–68. Trans Tech Publ, 2010.

[82] H-J Bunge. Texture analysis in materials science: mathematical methods. Elsevier, 2013.

[83] X Wu, G Proust, M Knezevic, and SR Kalidindi. Elastic–plastic property closures for hexagonal close-packed polycrystalline metals using first-order bounding theories. Acta Materialia, 55(8):2729–2737, 2007.

[84] H. Asgari, J. A. Szpunar, and A. G. Odeshi. Texture evolution and dynamic mechanical behavior of cast AZ magnesium alloys under high strain rate compressive loading. Materials and Design, 61:26–34, September 2014. ISSN 1873-4197. doi: 10.1016/j.matdes.2014.04.049.

[85] Mohsen Taheri Andani, Aaditya Lakshmanan, Veera Sundararaghavan, John Allison, and Amit Misra. Quantitative study of the effect of grain boundary parameters on the slip system level hall-petch slope for basal slip system in mg-4al. Acta Materialia, 200:148–161, 2020.

[86] H. Fujita and T. Tabata. The effect of grain size and deformation sub-structure on mechanical properties of polycrystalline aluminum. Acta Metallurgica, 21(4):355–365, April 1973. ISSN 0001-6160. doi: 10.1016/0001-6160(73)90191-0.

[87] N Ono, K Nakamura, and S Miura. Influence of grain boundaries on plastic deformation in pure Mg and AZ31 Mg alloy polycrystals. Materials Science Forum, 419-4:195–200, 2003. ISSN 0255-5476. URL https://www.cheric.org/research/tech/periodicals/view.php?seq=1254063.

[88] Lili Guo, Zhongchun Chen, and Li Gao. Effects of grain size, texture and twinning on mechanical properties and work-hardening behavior of AZ31 magnesium alloys. Materials Science and Engineering A, 528(29-30):8537–8545, November 2011. ISSN 0921-5093. doi: 10.1016/j.msea.2011.07.076.

[89] Yasumasa Chino, Mamoru Mabuchi, Ryuji Kishihara, Hiroyuki Hosokawa, Yasuo Yamada, Cui’e Wen, Koji Shimojima, and Hajime Iwasaki. Mechanical Properties and Press Formability at Room Temperature of AZ31 Mg Alloy Processed by Single Roller Drive Rolling. Materials Transactions, 43(10):2554–2560, 2002. ISSN 1345-9678. doi: 10.2320/matertrans.43.2554.

[90] J. A. del Valle, F. Carreño, and O. A. Ruano. Influence of texture and grain size on work hardening and ductility in magnesium-based alloys processed by ECAP and rolling. Acta Materialia, 54(16):4247–4259, September 2006. ISSN 1359-6454. doi: 10.1016/j.actamat.2006.05.018.

[91] L. B. Tong, M. Y. Zheng, S. Kamado, D. P. Zhang, J. Meng, L. R. Cheng, and H. J. Zhang. Reducing the tension-compression yield asymmetry of extruded Mg-Zn-Ca alloy via equal channel angular pressing. Journal of Magnesium and Alloys, 3(4):302–308, December 2015. ISSN 2213-9567. doi: 10.1016/j.jma.2015.08.007.

[92] Qian Yu, Zhi Wei Shan, Ju Li, Xiaoxu Huang, Lin Xiao, Jun Sun, and Evan Ma. Strong crystal size effect on deformation twinning. Nature, 463(7279):335–338, January 2010. ISSN 0028-0836. doi: 10.1038/nature08692. URL https://www.nature.com/articles/nature08692.

[93] N. Stanford, U. Carlson, and M. R. Barnett. Deformation twinning and the Hall-Petch relation in commercial purity Ti. Metallurgical and Materials Transactions a: Physical Metallurgy and Materials Science, 39 A(4):934–944, April 2008. ISSN 1073-5623. doi: 10.1007/s11661-007-9442-9.

[94] Ehab El-Danaf, Surya R. Kalidindi, and Roger D. Doherty. Influence of grain size and stacking-fault energy on deformation twinning in fcc metals. Metallurgical and Materials Transactions a: Physical Metallurgy and Materials Science, 30(5):1223–1233, 1999. ISSN 1073-5623. doi: 10.1007/s11661-999-0272-9.

[95] DL Atwell, MR Barnett, and WB Hutchinson. The effect of initial grain size and temperature on the tensile properties of magnesium alloy az31 sheet. Materials Science and Engineering: A, 549:1–6, 2012.

[96] V Kaushik, R Narasimhan, and RK Mishra. Experimental study of fracture behavior of magnesium single crystals. Materials Science and Engineering: A, 590:174–185, 2014.

[97] Daisuke Ando, Junichi Koike, and Y Sutou. The role of deformation twinning in the fracture behavior and mechanism of basal textured magnesium alloys. Materials Science and Engineering: A, 600:145–152, 2014.

[98] Michael J Nemcko, Hua Qiao, Peidong Wu, and David S Wilkinson. Effects of void fraction on void growth and linkage in commercially pure magnesium. Acta Materialia, 113:68–80, 2016.

[99] Michael J Nemcko and David S Wilkinson. Impact of microstructure on void growth and linkage in pure magnesium. International Journal of Fracture, 200(1-2):31–47, 2016.

[100] Michael J Nemcko, Jing Li, and David S Wilkinson. Effects of void band orientation and crystallographic anisotropy on void growth and coalescence. Journal of the Mechanics and Physics of Solids, 95:270–283, 2016.

[101] Michael J Nemcko and David S Wilkinson. On the damage and fracture of commercially pure magnesium using x-ray microtomography. Materials Science and Engineering: A, 676: 146–155, 2016.

[102] AA Benzerga. A theory for designing ductile materials with anisotropy. In Magnesium Technology 2019, pages 359–362. Springer, 2019.

[103] Joel B Stewart and Oana Cazacu. Analytical yield criterion for an anisotropic material containing spherical voids and exhibiting tension–compression asymmetry. International Journal of Solids and Structures, 48(2):357–373, 2011.

[104] Shamik Basu, E. Dogan, B. Kondori, I. Karaman, and A.A. Benzerga. Towards designing anisotropy for ductility enhancement: A theory-driven investigation in Mg-alloys. Acta Materialia, 131:349–362, 2017. ISSN 1359-6454. doi: 10.1016/j.actamat.2017.02.046. URL http://www.sciencedirect.com/science/article/pii/S1359645417301374.

[105] Benoit Revil-Baudard, Oana Cazacu, Philip Flater, Nitin Chandola, and JL Alves. Unusual plastic deformation and damage features in titanium: Experimental tests and constitutive modeling. Journal of the Mechanics and Physics of Solids, 88:100–122, 2016.

[106] Oana Cazacu, Benoit Revil-Baudard, and Nitin Chandola. Plasticity-damage couplings: from single crystal to polycrystalline materials. Springer, 2019.

[107] Padmeya P. Indurkar and Shailendra P. Joshi. Void Growth and Coalescence in Porous Plastic Solids With Sigmoidal Hardening. Journal of Applied Mechanics, 86(9), June 2019. ISSN 0021-8936. doi: 10.1115/1.4043519. 091001.

[108] S Baweja, PP Indurkar, and SP Joshi. On the role of crystallographic anisotropy and texture in damage tolerance of magnesium and its alloys. In Magnesium Technology 2021, page Accepted for Publication. Springer, 2021.